Computer Methods in Applied Mechanics and Engineering 449 (2026) 118513

Contents lists available at ScienceDirect

Comput. Methods Appl. Mech. Engrg.

journal homepage: www.elsevier.com/locate/cma

Fourth-order isogeometric phase-field modeling of dynamic brittle fracture: Numerical study and comparison with second-order models

L. Greco [a,*], J. Kiendl [b], M. Negri [c], A. Patton [b], A. Reali [a]

[a] Department of Civil engineering and Architecture, University of Pavia, via A. Ferrata 3, Pavia, 27100, Italy
[b] Department of Civil Engineering and Environmental sciences, Universität der Bundeswehr München, Werner-Heisenberg-Weg 39, Neubiberg, 85577, Germany
[c] Department of Mathematics, University of Pavia, via A.Ferrata 5, Pavia, 27100, Italy

ARTICLE INFO

Keywords:
Dynamic brittle fracture
Isogeometric analysis
Phase-field modeling
High-order models

ABSTRACT

We provide a thorough numerical investigation on phase-field simulations for dynamic brittle fracture; our analysis focuses on numerical performance, in terms of computational time and accuracy, measured by quantitative physical properties: energy conservation, crack speed, and critical stress. Simulations are performed by means of a semi-implicit staggered scheme, combining a Newmark method with the Projected Successive Over-Relaxation algorithm. This coupling ensures both an accurate solution of the elasto-dynamic equation and an effective solution of the linear complementarity problem, arising in the evolution of the phase-field parameter. In particular, with the Newmark method numerical dissipation is almost negligible; as a result, energy is conserved and simulations feature a remarkable representation of P and S waves, which irradiate from the boundary condition and from the tip, reflect on the boundary and interact with each other.

While accuracy requires both small time increments and small mesh sizes, which easily lead to unaffordable computational time, we employ a fourth order AT1 functional that allows (as a rule of thumb) to halve the mesh size, and then halve the time increment. This multiplicative effect produces a remarkable saving of computational time (up to the order of 90%) without compromising the quality of the results. Moreover, AT1 functionals, compared with AT2, feature a sharp value of the critical stress and sharper damage profiles and showcase in all results a gain in accuracy.

We employ an isogeometric framework that yields a straightforward discretization of the higher-order operators. First, we provide a calibration of the weight in front of the higher-order term, balancing the trade-off between accuracy and computational cost. Then, we compare the results obtained with second- and fourth-order AT1 and AT2 energies, using a few benchmark setups designed to focus the analysis on specific computational and physical aspects.

* Corresponding author.
E-mail addresses: luigi.greco@unipv.it (L. Greco), josef.kiendl@unibw.de (J. Kiendl), matteo.negri@unipv.it (M. Negri), alessia.patton@unibw.de (A. Patton), alessandro.reali@unipv.it (A. Reali).

https://doi.org/10.1016/j.cma.2025.118513
Received 24 June 2025; Received in revised form 26 September 2025; Accepted 20 October 2025
0045-7825/© 2025 The Author(s). Published by Elsevier B.V. This is an open access article under the CC BY license (http://creativecommons.org/licenses/by/4.0/).

1. Introduction

Fracture-related failure in structural systems often leads to severe economic and safety consequences. Accurate modeling of such phenomena is thus crucial, not only in quasi-static, but also under dynamics loading. Griffith's pioneering work [1] introduced an energetic criterion for crack propagation based on the energy release rate G and was later extended by Irwin through the notion of stress intensity factors [2]. Building on the energetic framework, Bourdin et al. [3] proposed a phase-field regularization of fracture, recasting the problem into a continuous setting. The two main regularizations, AT1 and AT2, stem from the work of Ambrosio and Tortorelli [4]. In general, AT1 functionals possess a well-defined elastic limit and narrow, finite transition regions that ensure a damage profile in $[0, 1]$, as opposed to AT2 models.

In the context of AT2 regularization, Borden et al. [5] originally introduced high-order functionals, conveniently discretized in an isogeometric analysis (IGA) [6] framework. These models entail similar accuracy to low-order ones, but allow for larger mesh sizes in their discretization and a consequent reduction of the computational cost. The recent work of [7] proposes instead a novel 4th-order AT1 model that combines the desired physical properties of AT1 in a higher-order formulation and offers the possibility to balance the trade-off between accuracy and computational cost through specific choices of the dissipation functional coefficients.

While initially developed for quasi-static regimes, phase-field approaches have been extended to dynamic fracture and AT2 regularization, starting with the work of Borden et al. [8], who incorporated inertial effects into the formulation. This extension poses numerical challenges, particularly regarding time integration. Within either a monolithic or a staggered approach (see, e.g., [9]), implicit schemes (such as the generalized-α [10]) and explicit variants, among which we recall [11] and the half-step explicit method in [12], are both used, but stability and energy conservation remain nontrivial points due to the nonlinearity and irreversibility of damage evolution. Monolithic approaches simultaneously solve the system of coupled differential equations; they have high convergence rates but typically exhibits convergence issues, especially at highly nonlinear load steps.

Conversely, staggered schemes, alternatively minimizing the total energy functional in the displacement and phase-field, prove to be robust, but show a slow rate of convergence. As in explicit approaches there is no control over convergence after each iteration and very refined load steps are needed for accuracy, we turn our attention to implicit schemes within a staggered approach, focusing instead on accuracy evaluation.

Besides the algorithmic standpoint, other works explore dynamic physical effects in more detail. For instance, Schlüter et al. [13] analyzed stress wave–fracture interactions, highlighting the role of free energy splits on wave interaction with fracture, and inertial effects on nucleation. Li et al. [14,15] studied the mesh-dependent numerical amplification effects over the fracture toughness and numerically computed a conventional dynamic energy release rate, verified as a tool to translate gradient damage mechanics results in fracture mechanics terminology. Mandal et al. [16] compared phase-field and cohesive zone models, analyzing the role of the kinetic energy in the energy release rate as a post-processing step.

From the provided literature scenario, it is clear that most dynamic phase-field studies are limited to 2nd-order models only. To the best of our knowledge, a comprehensive numerical study of high-order AT1 and AT2 formulations in dynamics is yet not present in the literature. Therefore, this work aims at filling this gap and provides an in-depth numerical investigation on phase-field with a focus on dynamic brittle fracture. Particular attention is paid to the choice of an accurate, energy-consistent time integration of the problem, minimising numerical dissipation without overdamping crack waves. To this end, we opt for a semi-implicit staggered scheme, combining a Newmark method to solve the balance of momentum equation and, to rigorously solve the phase-field problem, the Projected Successive Over-Relaxation algorithm (PSOR) [17] used for the first time in a dynamic framework. First, we focus on the novel 4th-order AT1 model proposed in [7], discretized *via* IGA. Namely, we investigate the influence of the coefficient χ, weighting the higher-order term, on the integration scheme accuracy, measuring quantitative physical properties such as internal and dissipated energies, and crack length. A comparison of low- and high-order models follows, for both AT1 and AT2 regularization, using $\chi = 1/16$ in the case of the AT1 4th-order formulation.

We highlight that the choice of a Newmark method leads to an almost negligible dissipation and a remarkable representation of P and S waves, respectively captured by the dynamic crack branching and dynamic Single Edge Notched (SEN) shear tests. Given that accuracy necessitates both refined time increments and mesh sizes, often leading to prohibitive computational costs, we show that the fourth-order AT1 functional permits halving the mesh size and consequently halving the time increment. This entails substantial savings in computational time without compromising the quality of the results, confirming the "half-mesh size" rule of thumb for the higher-order models analyzed in [18] in the quasi-static case. We complete our numerical investigation studying the critical stress through the pure traction test. The structure of the paper is as follows: in Section 2 we introduce the dynamic continuum formulation. The weak form and strong form of the governing equations are detailed in Appendixs A and B, respectively. Spatial and temporal discretization strategies are presented in Section 3. Numerical results and comparisons between 2nd- and 4th-order models follow in Section 4. Further numerical insights on the principle of energy conservation and Griffith's criterion in dynamics, as well as the complete wave propagation evolution for the plain strain benchmarks modeled with the 4th-order AT1 model [7] can be found in Appendixs C and D, respectively. Conclusions and future work are discussed in Section 5.

2. Continuum formulation

We consider an elastic body $\Omega \subset \mathbb{R}^N$ (with $N = 2, 3$) with material density $\rho > 0$ in a time interval $[0, T]$ and denote by $\mathbf{u}(\mathbf{x}, t)$, $\dot{\mathbf{u}}(\mathbf{x}, t)$, and $\ddot{\mathbf{u}}(\mathbf{x}, t)$ the displacement, velocity, and acceleration of the body for $\mathbf{x} \in \Omega$ and $t \in [0, T]$. On the boundary $\partial\Omega$, we consider Dirichlet boundary conditions $\mathbf{u}(\mathbf{x}, t) = \mathbf{g}(\mathbf{x}, t)$ on $\partial\Omega_D \subseteq \partial\Omega$ and Neumann boundary conditions $\boldsymbol{\sigma}(\mathbf{x}, t)\boldsymbol{\nu}(\mathbf{x}) = \mathbf{f}(\mathbf{x}, t)$ on $\partial\Omega_N \subseteq \partial\Omega$, such that $\partial\Omega_D \cup \partial\Omega_N = \partial\Omega$, $\partial\Omega_D \cap \partial\Omega_N = \emptyset$, whereas $\boldsymbol{\nu}$ is the outer unit normal and $\boldsymbol{\sigma}$ denotes the stress tensor (consistently derived from

the free energy in the following of the section). Finally, we introduce the phase-field variable $d(\mathbf{x},t)$, which takes values in $[0,1]$ and interpolates the unbroken (i.e., $d=0$) and fully broken (namely, $d=1$) states of the material.

Hereinafter, whenever possible, we omit the dependence of all the quantities on space and time, for simplicity of notation, and detail the energy functionals introducing, first, the kinetic energy of the body, given by

$$\mathcal{K}(\dot{\mathbf{u}}) = \int_\Omega \tfrac{1}{2}\,\rho\,\dot{\mathbf{u}}\cdot\dot{\mathbf{u}}\,\mathrm{d}\Omega, \tag{1}$$

that does not depend on the phase-field variable d. Then, we write the elastic energy in terms of the deviatoric and volumetric parts of the strain tensor $\boldsymbol{\varepsilon}=\boldsymbol{\varepsilon}(\mathbf{u})$, given respectively by $\boldsymbol{\varepsilon}_d=\boldsymbol{\varepsilon}-\boldsymbol{\varepsilon}_v$ and $\boldsymbol{\varepsilon}_v=\varepsilon_v\boldsymbol{I}$, being $\varepsilon_v=\frac{1}{N}\boldsymbol{\varepsilon}:\boldsymbol{I}$. Thus, following [19], we split the elastic energy density as

$$\psi_e(\boldsymbol{\varepsilon},d) = w(d)\,\psi_e^+(\boldsymbol{\varepsilon}) + \psi_e^-(\boldsymbol{\varepsilon}), \tag{2}$$

where $w(d)=((1-d)^2+\eta)$ is the degradation function, η is a factor (i.e., $0<\eta\ll 1$) to maintain a residual stiffness in the fully broken case, while the positive and negative portions of the elastic energy density are defined as

$$\psi_e^+(\boldsymbol{\varepsilon}) = \tfrac{1}{2}\big(\kappa[\varepsilon_v]_+^2 + \mu|\boldsymbol{\varepsilon}_d|^2\big), \qquad \psi_e^-(\boldsymbol{\varepsilon}) = \tfrac{1}{2}\kappa[\varepsilon_v]_-^2\,. \tag{3}$$

In Eq. (3), $[\cdot]_\pm$ denote the positive and negative parts of the strain tensor, whereas κ and μ are the bulk and the shear moduli, respectively. Clearly, the stress can be derived from the specific elastic energy as $\boldsymbol{\sigma}=\boldsymbol{\sigma}(\mathbf{u},d)=\partial_{\boldsymbol{\varepsilon}}\psi_e(\boldsymbol{\varepsilon}(\mathbf{u}),d)$. Then, the elastic energy is given by

$$\mathcal{E}(\mathbf{u},d) = \int_\Omega \psi_e(\boldsymbol{\varepsilon}(\mathbf{u}),d)\,\mathrm{d}\Omega, \tag{4}$$

whereas the usual work of external forces reads

$$\mathcal{W}^{\mathrm{ext}}(\mathbf{u},t) = \int_{\partial\Omega_N} \mathbf{f}(t)\cdot\mathbf{u}\,\mathrm{d}A\,. \tag{5}$$

In this work, we employ different types of phase-field fracture energy, which will be of the form $G_c\mathcal{F}(d)$, where $G_c>0$ is the toughness. Thus, for 2nd-order functionals the surface energy $\mathcal{F}$ is given in general by [3,4]

$$\mathcal{F}(d) = \int_\Omega \phi^{\mathrm{II}}(d,\nabla d)\,\mathrm{d}\Omega, \quad \phi^{\mathrm{II}}(d,\nabla d) = \frac{1}{c_\alpha l_0}\big(\alpha(d)+l_0^2|\nabla d|^2\big). \tag{6}$$

Here, $l_0>0$ is the internal length and $c_\alpha>0$ is a normalization parameter. In particular, we employ $\alpha(d)=d$ and $\alpha(d)=d^2$ corresponding to the so-called AT1 and AT2 functionals, respectively, such that we denote by $\phi^{\mathrm{II}}_{\mathrm{AT1}}$ and $\phi^{\mathrm{II}}_{\mathrm{AT2}}$ the corresponding energy densities. In the former case, we set $c_\alpha=8/3$ while in the latter $c_\alpha=2$; these values of the normalization parameter are choosen in such a way that in the Γ-limit, as $l_0\to 0$, the crack length (in 2D) and the crack surface (in 3D) are recovered. For 4th-order functionals, the surface energy is then given by

$$\mathcal{F}(d) = \int_\Omega \phi^{\mathrm{IV}}(d,\nabla d,\Delta d)\,\mathrm{d}\Omega\,. \tag{7}$$

In this case, we employ [5,20]

$$\phi^{\mathrm{IV}}_{\mathrm{AT2}}(d,\nabla d,\Delta d) = \frac{1}{2l_0}\left(d^2 + \frac{l_0^2}{2}|\nabla d|^2 + \frac{l_0^4}{16}|\Delta d|^2\right) \tag{8}$$

and [7]

$$\phi^{\mathrm{IV}}_{\mathrm{AT1}}(d,\nabla d,\Delta d) = \frac{1}{c_\chi l_0}\big(d + l_0^2|\nabla d|^2 + \chi l_0^4|\Delta d|^2\big)\,. \tag{9}$$

Within functional (9), the regularization constant c_χ and the coefficient multiplying the Laplacian term χ are left generic. In fact, the values of the normalization parameter will be explicitly computed, as a function of the weight $\chi>0$, and utilized in the numerical tests (see Section 4), as recently proposed in [7]. Additionally, in Section 4.3 we will provide a parametric study to see the influence of c_χ coefficient on the numerical results.

At this point, we can introduce the potential energy Ψ and the Lagrangian $\mathscr{L}$

$$\Psi(\mathbf{u},d) = \mathcal{E}(\mathbf{u},d) - \mathcal{W}^{\mathrm{ext}}(\mathbf{u},t) + G_c\mathcal{F}(d), \quad \mathscr{L}(\mathbf{u},\dot{\mathbf{u}},d) = \mathcal{K}(\dot{\mathbf{u}}) - \Psi(\mathbf{u},d), \tag{10}$$

as well as the action $\mathcal{A}$ of the system, given by

$$\mathcal{A}(\mathbf{u},d) = \int_0^T \mathscr{L}(\mathbf{u}(t),\dot{\mathbf{u}}(t),d(t))\,\mathrm{d}t\,. \tag{11}$$

Thus, the equations of motion are derived from: the principle of stationary action, given the phase-field d; the stationarity of the potential energy, given the displacement $\mathbf{u}$; and the principle of conservation of energy, i.e.,

$$\frac{\partial\mathcal{A}}{\partial\mathbf{u}}(\mathbf{u},d)[\delta\mathbf{u}] = 0, \qquad \frac{\partial\Psi}{\partial d}(\mathbf{u}(t),d(t))[\delta d] \geq 0,\ \dot{d}(t)\geq 0, \qquad \frac{\mathrm{d}}{\mathrm{d}t}\Big(\mathcal{K}(\dot{\mathbf{u}}(t)) + \Psi\big(\mathbf{u}(t),d(t)\big)\Big) = 0\,. \tag{12}$$

We remark that, in the evolution, the phase-field variable is constrained to be non-decreasing in time to model the irreversibility of the crack, and, therefore, the admissible variations of d must satisfy $\delta d \geq 0$. As a consequence, the equilibrium of the potential energy with respect to d is unilateral, and thereby characterized by an inequality. After some manipulations, the conditions (12), in variational form, read

$$\frac{\mathrm{d}}{\mathrm{d}t}\Big(\frac{\partial \mathscr{L}}{\partial \dot{\mathbf{u}}}\big(\mathbf{u}(t),\dot{\mathbf{u}}(t),d(t)\big)\Big)[\delta\mathbf{u}] - \frac{\partial \mathscr{L}}{\partial \mathbf{u}}\big(\mathbf{u}(t),\dot{\mathbf{u}}(t),d(t)\big)[\delta\mathbf{u}] = 0,$$

that is

$$\frac{\mathrm{d}}{\mathrm{d}t}\Big(\frac{\partial \mathcal{K}}{\partial \dot{\mathbf{u}}}\big(\dot{\mathbf{u}}(t)\big)\Big)[\delta\mathbf{u}] + \frac{\partial \Psi}{\partial \mathbf{u}}\big(\mathbf{u}(t),d(t)\big)[\delta\mathbf{u}] = 0, \tag{13}$$

together with

$$\frac{\partial \Psi}{\partial d}\big(\mathbf{u}(t),d(t)\big)[\delta d] \geq 0, \quad \frac{\partial \Psi}{\partial d}\big(\mathbf{u}(t),d(t)\big)[\dot{d}(t)] = 0, \quad \dot{d}(t) \geq 0, \tag{14}$$

whereas their explicit integral representation and strong form evolution are provided in A and B, respectively, distinguishing between 2nd- and 4th-order formulations.

3. Space and time discretization

Let us start with the discetization in space and consider a Galerkin isogeometric approach with C^1-continuous quadratic shape functions (see, e.g., [6,21,22]), that allows the approximation of the Laplacian operator in Eqs. (8) and (9).

Thus, we denote by $R_i^{\mathbf{u}} = R_i^d = R_i : \Omega \to \mathbb{R}$ the isogeometric shape functions for the approximation of both the displacement $\mathbf{u}$ and the phase-field parameter d. Consequently, the approximate displacement field $\mathbf{u}_h$ and phase-field variable d_h are given by a linear combination of IGA shape functions and either displacement, $\hat{\mathbf{u}}_i \in \mathbb{R}^3$, or order parameter, $\hat{d}_i \in \mathbb{R}$, control variables, respectively, as

$$\begin{aligned} \mathbf{u}(\mathbf{x},t) \approx \mathbf{u}_h(\mathbf{x},t) &= \sum_i^{\mathrm{n_{sf}}} R_i^{\mathbf{u}}(\mathbf{x})\,\hat{\mathbf{u}}_i(t) = \sum_i^{\mathrm{n_{sf}}} R_i(\mathbf{x})\,\hat{\mathbf{u}}_i(t), \\ d(\mathbf{x},t) \approx d_h(\mathbf{x},t) &= \sum_i^{\mathrm{n_{sf}}} R_i^{d}(\mathbf{x})\,\hat{d}_i(t) = \sum_i^{\mathrm{n_{sf}}} R_i(\mathbf{x})\,\hat{d}_i(t), \end{aligned} \tag{15}$$

where $\mathrm{n_{sf}}$ is the total number of shape functions pertaining to the space discretization. Thus, velocity and acceleration are obtained, respectively, taking the first and second time derivative of Eq. $(15)_1$ as

$$\dot{\mathbf{u}}(\mathbf{x},t) \approx \dot{\mathbf{u}}_h(\mathbf{x},t) = \sum_i^{\mathrm{n_{sf}}} R_i(\mathbf{x})\,\hat{\mathbf{v}}_i(t), \qquad \ddot{\mathbf{u}}(\mathbf{x},t) \approx \ddot{\mathbf{u}}_h(\mathbf{x},t) = \sum_i^{\mathrm{n_{sf}}} R_i(\mathbf{x})\,\hat{\mathbf{a}}_i(t), \tag{16}$$

where $\hat{\mathbf{v}}_i(t)$ and $\hat{\mathbf{a}}_i(t)$ respectively are the velocity and acceleration control variables. Then, we substitute the approximations (15) and (16) in the weak form of the elasto-dynamic system (13) and in the Karush-Kuhn-Tucker conditions (14), whose integral representation is provided in the Appendix A. Subsequently, we consider a uniform time discretization $t_n = n\Delta t$ (with step $\Delta t > 0$ and $n \in \mathbb{N}_0^+$) and introduce the notation $\mathbf{u}_n$ to denote the $\mathrm{n_{sf}} \times N$ vector of the displacement parameters $\hat{\mathbf{u}}_i$ at time t_n. In a similar way, we denote by $\dot{\mathbf{u}}_n$ and $\ddot{\mathbf{u}}_n$ the time discretizations of velocity and acceleration for the $\mathrm{n_{sf}} \times N$ vector of displacement $\mathbf{u}_n$. Finally, $\boldsymbol{d}_n$ denotes the $\mathrm{n_{sf}}$ vector of the phase-field parameters $\hat{d}_i$ at time t_n. Thus, we adopt a backward Euler time integration of the phase-field rate, i.e., $\boldsymbol{d}_{n+1} = \boldsymbol{d}_n + \Delta\boldsymbol{d}$. In these terms, the time discretization of the variational formulation of the coupled problem (13)-(14) can be rewritten in matrix form as

$$\begin{cases} \mathbf{M}\,\ddot{\mathbf{u}}_{n+1} + \mathbf{K}(\mathbf{u}_{n+1},\boldsymbol{d}_{n+1})\,\mathbf{u}_{n+1} - \mathbf{F}^{\text{ext}}_{n+1} = \mathbf{0}\,, \\ \mathbf{Q}^{\text{II,IV}}(\mathbf{u}_{n+1})\,\Delta\boldsymbol{d} - \mathbf{q}^{\text{II,IV}}(\mathbf{u}_{n+1},\boldsymbol{d}_n) \geq \mathbf{0}, \\ \big(\mathbf{Q}^{\text{II,IV}}(\mathbf{u}_{n+1})\,\Delta\boldsymbol{d} - \mathbf{q}^{\text{II,IV}}(\mathbf{u}_{n+1},\boldsymbol{d}_n)\big)\cdot\Delta\boldsymbol{d} = 0, \quad \Delta\boldsymbol{d} \geq 0\,. \end{cases} \tag{17}$$

For the definition of matrices $\mathbf{K}$, $\mathbf{Q}$, and vector $\mathbf{q}$ we refer the interested reader to Sections 4.2 and 4.3 in [17] and to [7,18], while the mass matrix $\mathbf{M}$ entries read

$$\mathrm{M}_{ij} = \int_\Omega \rho\, R_i R_j \,\mathrm{d}\Omega\,.$$

To advance in time, we consider essentially a staggered semi-implicit scheme (see Algorithm 1), which combines a Newmark average acceleration time integration method, for the solution of the elasto-dynamic Eq. $(17)_1$, with the PSOR algorithm [17,23] to tackle the linear phase-field complementarity problem $(17)_2$-$(17)_3$. The choice of the Newmark method for the time integration of the mechanical part minimizes the artificial numerical dissipation, unlike what is commonly adopted in the reference literature (see for instance the generalized-α scheme in Borden et al. [8]). As it will be shown in Section 4.2, this decision has significant implications for both crack propagation dynamics and wave propagation within the domain.

Entering more in detail with respect to the staggered algorithm steps, the sequences $\mathbf{u}^i_{n+1}, \dot{\mathbf{u}}^i_{n+1}, \ddot{\mathbf{u}}^i_{n+1}$, and $\boldsymbol{d}^i_{n+1}$ (for an iteration $i \geq 0$) are computed until the following exit criterion is met:

$$\mathrm{Res}_{\text{stag}} = \|\mathbf{R}^i_{n+1}\|/\|\mathbf{R}^0_{n+1}\| < \mathrm{Tol}_{\text{stag}}, \tag{18}$$

Algorithm 1 Staggered scheme for the solution of the incremental problem at step $n+1$.

Require: solution $\mathbf{u}_n, \dot{\mathbf{u}}_n, \ddot{\mathbf{u}}_n, \boldsymbol{d}_n$ and boundary conditions $\mathbf{f}_{n+1}, \mathbf{g}_{n+1}$
1: set $i = 0$
2: **Predictor:** initialize $\mathbf{u}^i_{n+1}, \dot{\mathbf{u}}^i_{n+1}, \ddot{\mathbf{u}}^i_{n+1}, \boldsymbol{d}^i_{n+1}$ by Eq. (19) and Res_{stag} *via* Eq. (18)
3: **while** $\text{Res}_{\text{stag}} \geq \text{TOL}_{\text{stag}}$ **do**
4: $i \to i+1$
5: **Newmark step:** given $\boldsymbol{d}^i_{n+1}$ find $\mathbf{u}^{i+1}_{n+1}, \dot{\mathbf{u}}^{i+1}_{n+1}, \ddot{\mathbf{u}}^{i+1}_{n+1}$ using Eqs. (22), (23), (24) (**Multicorrector**), once known $\Delta\mathbf{u}^{i+1}$ (Newton-Raphson substep *via* Eq. (20))
6: **PSOR step:** given $\boldsymbol{u}^{i+1}_{n+1}$ find $\Delta\boldsymbol{d}^{i+1}$ using Eqs. (25) and update $\boldsymbol{d}^{i+1}_{n+1}$
7: update $\mathbf{R}^{i+1}_{n+1}$ and Res_{stag}
8: **end while**
9: $(\mathbf{u}_{n+1}, \dot{\mathbf{u}}_{n+1}, \ddot{\mathbf{u}}_{n+1}, \boldsymbol{d}_{n+1}) \to \mathbf{u}^{i+1}_{n+1}, \dot{\mathbf{u}}^{i+1}_{n+1}, \ddot{\mathbf{u}}^{i+1}_{n+1}, \boldsymbol{d}^{i+1}_{n+1}$
Ensure: $(\mathbf{u}_{n+1}, \dot{\mathbf{u}}_{n+1}, \ddot{\mathbf{u}}_{n+1}, \boldsymbol{d}_{n+1})$

where $\mathbf{R}^i_{n+1} := \mathbf{M}\ddot{\mathbf{u}}^i_{n+1} + \mathbf{K}(\mathbf{u}^i_{n+1}, \boldsymbol{d}^i_{n+1})\mathbf{u}^i_{n+1} - \mathbf{F}^{\text{ext}}_{n+1}$ and $\text{Tol}_{\text{stag}} = 1 \cdot 10^{-5}$. Following [24], the predictor solution (corresponding to the index $i = 0$) is defined as

$$\dot{\mathbf{u}}^0_{n+1} = \dot{\mathbf{u}}_n, \qquad \ddot{\mathbf{u}}^0_{n+1} = \frac{\gamma - 1}{\gamma}\ddot{\mathbf{u}}_n, \qquad \mathbf{u}^0_{n+1} = \mathbf{u}_n + \Delta t\, \dot{\mathbf{u}}_n + \frac{(\Delta t)^2}{2}\Big((1-2\beta)\ddot{\mathbf{u}}_n + 2\beta\ddot{\mathbf{u}}^0_{n+1}\Big), \qquad \boldsymbol{d}^0_{n+1} = \boldsymbol{d}_n, \tag{19}$$

where the considered values of the Newmark's constants are $\gamma = 1/2$ and $\beta = 1/4$. Within the Newmark's step, we perform additional Newton–Raphson iterations for a fixed phase field solution $\boldsymbol{d}^i_{n+1}$, such that we use the residual to compute the displacement correction $\Delta\mathbf{u}^{i+1}_{n+1}$ by solving:

$$\mathbf{K}^* \Delta\mathbf{u}^{i+1}_{n+1} = -\mathbf{R}^i_{n+1}, \tag{20}$$

where

$$\mathbf{K}^* = \frac{1}{\beta(\Delta \mathrm{t})^2}\mathbf{M} + \mathbf{K}(\mathbf{u}^i_{n+1}, \boldsymbol{d}^i_{n+1}). \tag{21}$$

Next, the correction phase is applied to update the solution as follows:

$$\mathbf{u}^{i+1}_{n+1} = \mathbf{u}^i_{n+1} + \Delta\mathbf{u}^{i+1}_{n+1}, \tag{22}$$

$$\dot{\mathbf{u}}^{i+1}_{n+1} = \left(\frac{\gamma}{\beta\Delta \mathrm{t}}\right)(\mathbf{u}^{i+1}_{n+1} - \mathbf{u}^i_n) + \left(1 - \frac{\gamma}{\beta}\right)\dot{\mathbf{u}}^i_n + \left[\Delta \mathrm{t}\left(1 - \frac{\gamma}{2\beta}\right)\right]\ddot{\mathbf{u}}^i_n, \tag{23}$$

$$\ddot{\mathbf{u}}^{i+1}_{n+1} = \left(\frac{1}{\beta(\Delta \mathrm{t})^2}\right)(\mathbf{u}^{i+1}_{n+1} - \mathbf{u}^i_n) - \left(\frac{1}{\beta\Delta \mathrm{t}}\right)\dot{\mathbf{u}}^i_n - \left(\frac{1}{2\beta} - 1\right)\ddot{\mathbf{u}}^i_n. \tag{24}$$

Then, after the solution of the mechanical part, we proceed with the next staggered sub-step by solving, for a fixed displacement solution $\mathbf{u}^{i+1}_{n+1}$, the phase-field problem

$$\mathbf{Q}^{\text{II,IV}}\,\Delta\boldsymbol{d}^{i+1}_{n+1} - \mathbf{q}^{\text{II,IV}} \geq \mathbf{0}, \quad \left(\mathbf{Q}^{\text{II,IV}}\,\Delta\boldsymbol{d}^{i+1}_{n+1} - \mathbf{q}^{\text{II,IV}}\right) \cdot \Delta\boldsymbol{d}^{i+1}_{n+1} = 0, \quad \Delta\boldsymbol{d}^{i+1}_{n+1} \geq 0, \tag{25}$$

where $\mathbf{Q}^{\text{II,IV}} = \mathbf{Q}^{\text{II,IV}}(\mathbf{u}^{i+1}_{n+1})$ and $\mathbf{q}^{\text{II,IV}} = \mathbf{q}^{\text{II,IV}}(\mathbf{u}^{i+1}_{n+1}, \boldsymbol{d}_n)$. Specifically, system (25) is rigorously solved by means of the PSOR algorithm and we refer the interest reader to [17] for further detail e.g., in terms of possible exit criteria of this method and suitable tolerance choices in a phase-field brittle fracture context.

Remark 1. A loosely staggered approach is employed, such that the convergence of the displacement-computation step, prior to solving the phase-field fracture problem, is verified by simultaneously checking the residual and the change in the displacement norm between two consecutive iterations (i.e., $\|\mathbf{u}^i_{n+1}\|/\|\mathbf{u}^0_{n+1}\| < \text{TOL}_{\text{u}}$, with $\text{TOL}_{\text{u}} = 1 \cdot 10^{-4}$ in the present case), thereby ensuring the accuracy of the mechanical response.

4. Numerical results

In this section, extensive numerical tests are conducted in an implicit dynamic framework. More specifically, we motivate first the choice of the Newmark method, as the time integration scheme for the mechanical problem, that leads to a minimal numerical dissipation, thereby allowing for an insightful representation of P and S waves. Subsequently, we analyze the 4th-order AT1 model applied in a dynamic setting: this represents a novel contribution of the present work, as the 4th-order AT1 formulation, recently proposed in [7], has so far been investigated in a quasi- static framework. To this end, we first focus on a parametric study to motivate the selection of the coefficient weighting the higher-order term, analyzing the influence of the latter on the integration algorithm accuracy.

Then, leveraging the computational advantages of high-order formulations [7,18], we compare, in implicit dynamics, low- and higher-order models, for both AT1 and AT2 formulations, investigating the behavior of the novel 4th-order AT1 formulation with respect to well-estabilished reference phase-field models. Finally, we study the critical stress under a pure traction test to complete our numerical investigation.

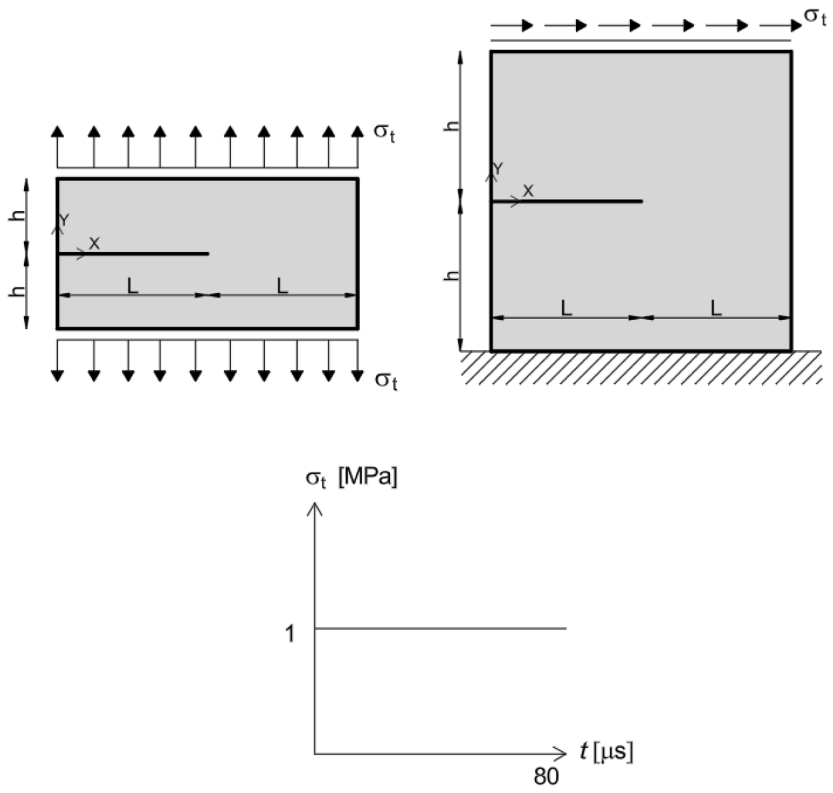

Fig. 1. Top row: geometry and boundary conditions of the dynamic crack branching test (left) and the dynamic SEN shear test (right). Bottom row: loading history.

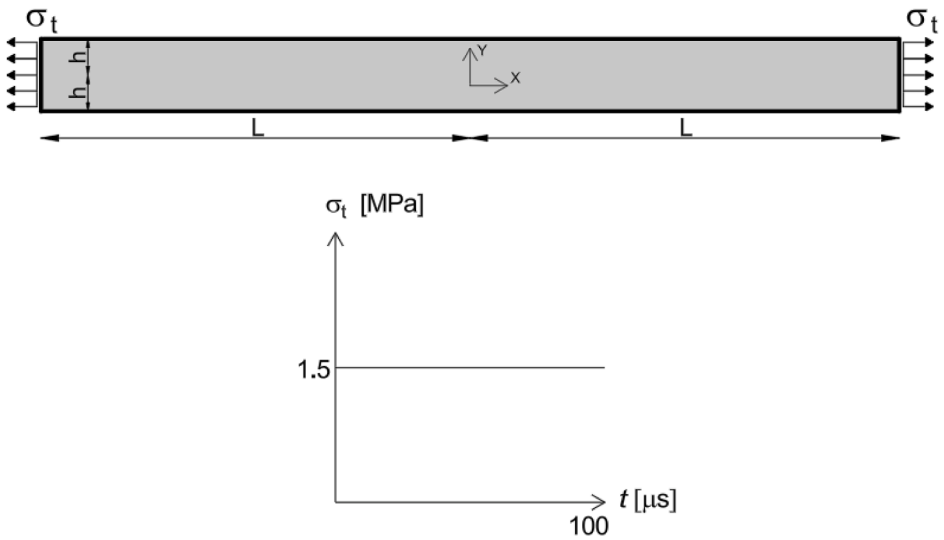

Fig. 2. Dynamic pure traction test: geometry, boundary conditions, and loading history.

4.1. Benchmarks description

In this section, we present the numerical benchmarks described in Figs. 1 and 2. All examined examples, namely, the Dynamic crack branching [8], the Dynamic SEN shear, and the Dynamic pure traction tests consider plain strain conditions. In the first two cases, the specimen is loaded by a constant stress with magnitude $\sigma_t = 1$ N/mm, as detailed in Fig. 1 and the total simulated time is T

Table 1
Geometrical and material properties of the considered tests.

Test	E [N/mm^2]	ν [–]	ρ [kg/mm^2]	G_c [N/mm]	l_0 [mm]	L [mm]	h [mm]
Dynamic crack branching	$32 \cdot 10^3$	0.2	$2.46 \cdot 10^{-9}$	$3 \cdot 10^{-3}$	$5 \cdot 10^{-1}$	50	20
Dynamic SEN shear	$32 \cdot 10^3$	0.2	$2.46 \cdot 10^{-9}$	$3 \cdot 10^{-3}$	$5 \cdot 10^{-1}$	50	50
Dynamic pure traction	$10 \cdot 10^3$	0	$2.46 \cdot 10^{-9}$	$3 \cdot 10^{-3}$	$5 \cdot 10^{-1}$	100	5

$= 80\,\mu s$. In the third one, the specimen is also loaded by a constant stress with magnitude $\sigma_t = 1.5$ N/mm, but over a total simulated time $T = 100\,\mu s$. All geometrical and material properties of the samples are reported in Table 1.

One of the aims of this work is to investigate how the choice of different phase-field models influences dynamic effects related to inertia, such as wave propagation. While a detailed theoretical analysis of such effects lies beyond the scope of this study, even the mere tracking of the wave fronts can provide, to some extent, insight into the behavior of the energy functionals (namely, the response of the system with respect to the energy split [13]) and time integration schemes with respect to numerical dissipation, as well as the visual interaction of the waves with the crack patterns in the evolution. Thus, following the approach in Roubíček et al. [25], P- and S-wave contributions are extracted from the velocity field *via* $\nabla \cdot \dot{\mathbf{u}}$ and $\nabla \times \dot{\mathbf{u}}$, respectively. Selected snapshots of the wave propagation, that either compare the wave response for Newmark and generalized-α schemes or focus on the wave propagation itself for the 4th-order AT1 formulation and reference literature models, are presented in the following sections. Finally, we provide additional time instances of the wave propagation for the plane strain configurations modeled *via* the 4th-order AT1 formulation in Appendix D.

4.2. Generalized-α and Newmark average acceleration method

In phase-field fracture dynamics literature, the generalized-α time integration scheme is commonly employed (see, e.g., [8]). This algorithm, formulated within a single-step multi-corrector framework, preserves unconditional stability for linear problems while introducing controllable high-frequency numerical dissipation. This artificial damping, governed by the parameters α_m and α_f, enhances the robustness of the time integration by attenuating spurious oscillations in the high-frequency range without compromising second-order accuracy for the low-frequency response. For the sake of readability and to exploit the descibed framework in Section 3, the generalized-α simply substitutes step No. 5 of Algorithm 1 and considers Eqs. (18)–(24) with the parameters β and γ defined instead as follows:

$$\beta = \frac{(1 + \alpha_m - \alpha_f)^2}{4}, \quad \gamma = \frac{1}{2} + \alpha_m - \alpha_f, \tag{26}$$

where α_m and α_f are defined as

$$\alpha_f = \frac{1}{\rho_\infty + 1}, \quad \alpha_m = \frac{2 - \rho_\infty}{\rho_\infty + 1}, \tag{27}$$

and the coefficient ρ_∞ represents the spectral radius of the amplification matrix as $\Delta t \to \infty$, such that, if $\rho_\infty = 1$, we get $\alpha_m = \alpha_f = 1/2$ (i.e., $\gamma = 1/2$ and $\beta = 1/4$), thus recovering the Newmark avarage acceleration algorithm. Then, in the multicorrector stage α_m and α_f constants are used to compute the residual $\mathbf{K}^*$ matrix of Eq. (20) as follows

$$\mathbf{K}^* = \frac{\alpha_m}{\beta(\Delta t)^2}\mathbf{M} + \alpha_f \mathbf{K}(\mathbf{u}^i_{n+1}, \boldsymbol{d}^i_{n+1}). \tag{28}$$

Finally, theα multi-correction is applied on the displacement, velocity, and acceleration:

$$\mathbf{u}^{(i+1),\alpha}_{n+1} = \alpha_f \mathbf{u}^{i+1}_{n+1} + (1 - \alpha_f)\mathbf{u}^i_n \longrightarrow \mathbf{u}^{(i+1)}_{n+1} = \mathbf{u}^{(i+1),\alpha}_{n+1}, \tag{29}$$

$$\dot{\mathbf{u}}^{(i+1),\alpha}_{n+1} = \alpha_f \dot{\mathbf{u}}^{i+1}_{n+1} + (1 - \alpha_f)\dot{\mathbf{u}}^i_n \longrightarrow \dot{\mathbf{u}}^{(i+1)}_{n+1} = \dot{\mathbf{u}}^{(i+1),\alpha}_{n+1}, \tag{30}$$

$$\ddot{\mathbf{u}}^{(i+1),\alpha}_{n+1} = \alpha_m \ddot{\mathbf{u}}^{i+1}_{n+1} + (1 - \alpha_m)\ddot{\mathbf{u}}^i_n \longrightarrow \ddot{\mathbf{u}}^{(i+1)}_{n+1} = \ddot{\mathbf{u}}^{(i+1),\alpha}_{n+1}. \tag{31}$$

In the following, we analyze the dynamic crack branching test response using the generalized-α method and investigate different values of ρ_∞ in Fig. 3. The results focus on the 2nd-order AT2 model, whereas we omit for the sake of brevity the response relative to the other low- and high-order AT-regularization, as they lead to the same considerations. In particular, we observe a delayed behavior in terms of crack propagation with respect to what has been observed in [8] for $\rho_\infty = 0.5$; however, this discrepancy can be attributed to several factors: a different energy decomposition, a different algorithm enforcing crack irreversibility, and a different solution scheme for the coupled problem. The reason why the value of ρ_∞ affects fracture propagation has never been investigated in detail and lies beyond the scope of this work. Hypothetically, a stronger damping of the waves leads to a slower stress redistribution at the crack tip, thereby resulting in higher stress concentration and, consequently, a faster crack propagation compared to the undamped case. In the sequel, a value of $\rho_\infty = 0.05$ is adopted to align the timing of fracture propagation with the reference simulation in [8]. Then, we compare in Fig. 4 the behavior of the waves for the two time integration schemes: the Newmark method (average acceleration) on the left and the generalized-α method on the right. Two distinct time instances are shown: (i) the initial waves radiating from the domain edges due to the applied load and (ii) the waves generated during crack propagation. As observed from

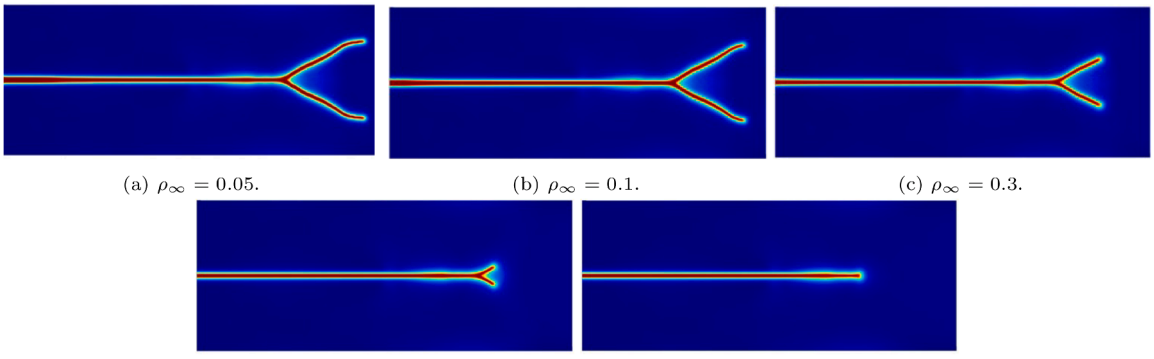

(a) $\rho_\infty = 0.05$. (b) $\rho_\infty = 0.1$. (c) $\rho_\infty = 0.3$.

(d) $\rho_\infty = 0.5$. (e) $\rho_\infty = 0.7$.

Fig. 3. Dynamic crack branching test: parametric study of the influence of the ρ_∞ coefficient on the fracture propagation for 2nd -order AT2 model, with fixed $\Delta t = 10^{-7}$ s and mesh size $h = l_0/2$. Crack pattern referred to time $T = 80$ μs.

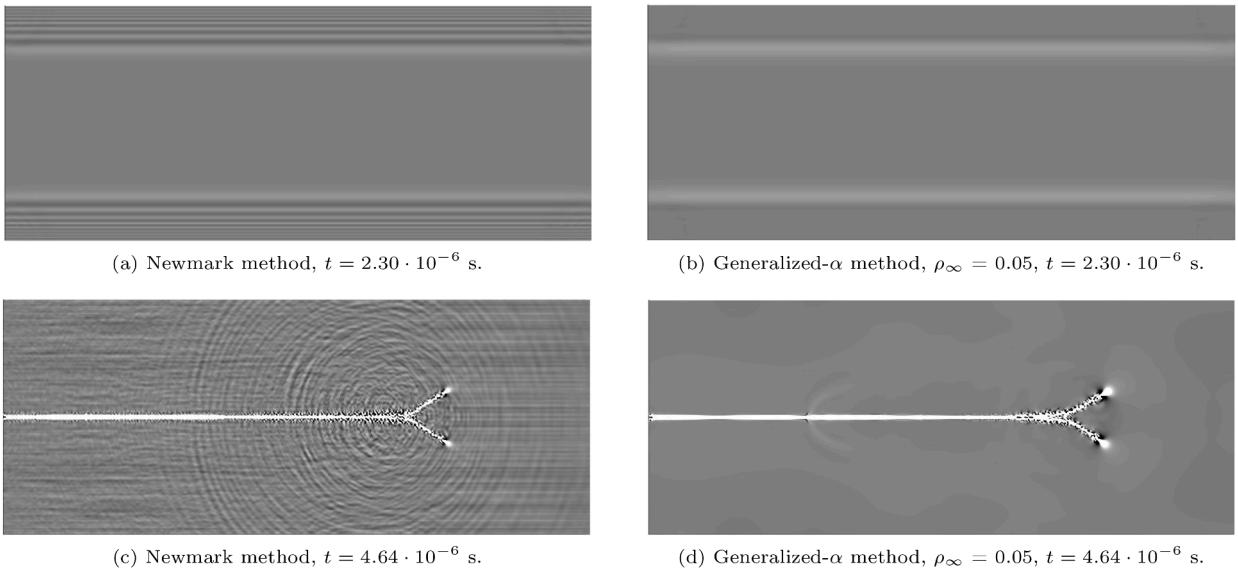

(a) Newmark method, $t = 2.30 \cdot 10^{-6}$ s. (b) Generalized-α method, $\rho_\infty = 0.05$, $t = 2.30 \cdot 10^{-6}$ s.

(c) Newmark method, $t = 4.64 \cdot 10^{-6}$ s. (d) Generalized-α method, $\rho_\infty = 0.05$, $t = 4.64 \cdot 10^{-6}$ s.

Fig. 4. Dynamic crack branching test for 2nd- order AT2 with fixed $\Delta t = 10^{-7}$ s and mesh size $h = l_0/2$: wave propagation comparison for Newmark method and generalized-α.

the body wave representation, the velocity field computed using the Newmark method yields a sharp and well-defined wavefront. In contrast, the generalized-α method produces a smeared front, where the wavefront is significantly less distinct. This effect is attributed to the inherent numerical dissipation introduced by the method, which attenuates the wave amplitude and increases the effective wavelength.

Therefore, given the above considerations, in the sequel all simulations will be performed using only the Newmark method.

4.3. 4th-order AT1 model: Parametric study on the coefficient χ

In this section, we study the influence of the parameter χ, appearing in Eq. (9), on the dynamic behavior of the dynamic crack branching and SEN shear tests (see Fig. 1). We consider $\chi \in (0, 1)$ as in the quasi-static setting [7]. Unless otherwise specified, this study is carried out for a fixed mesh size $h = l_0/2$ and a time step accordingly set to $\Delta t = h/v_R = 10^{-7}s$, following [8], where v_R is the Rayleigh wave speed.

4.3.1. Dynamic crack branching test

In Fig. 5, it can be observed how the coefficient χ influences the phase-field crack pattern. Namely, it can be noticed that the width of the damage profile increases as χ increases and, consequently, the degree of detail of the fracture representation changes. This is in accordance with the quasi-static setting, see in particular Section 2 of [7], where the support of the damage profile is

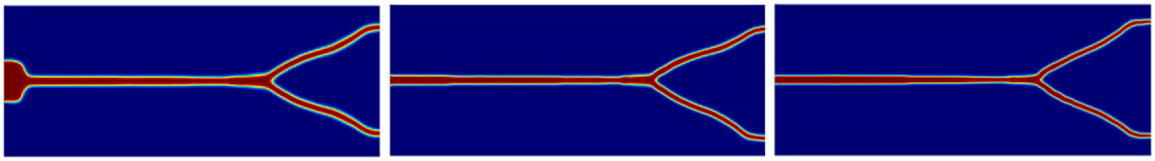

(a) $\chi = 1$. (b) $\chi = 1/4$. (c) $\chi = 1/16$.

Fig. 5. Dynamic crack branching test: parametric study of the influence of the χ coefficient on the fracture propagation for a fixed$\Delta t = 10^{-7}$ s and mesh size $h = l_0/2$. Crack patterns referred to time $T = 80$ μs.

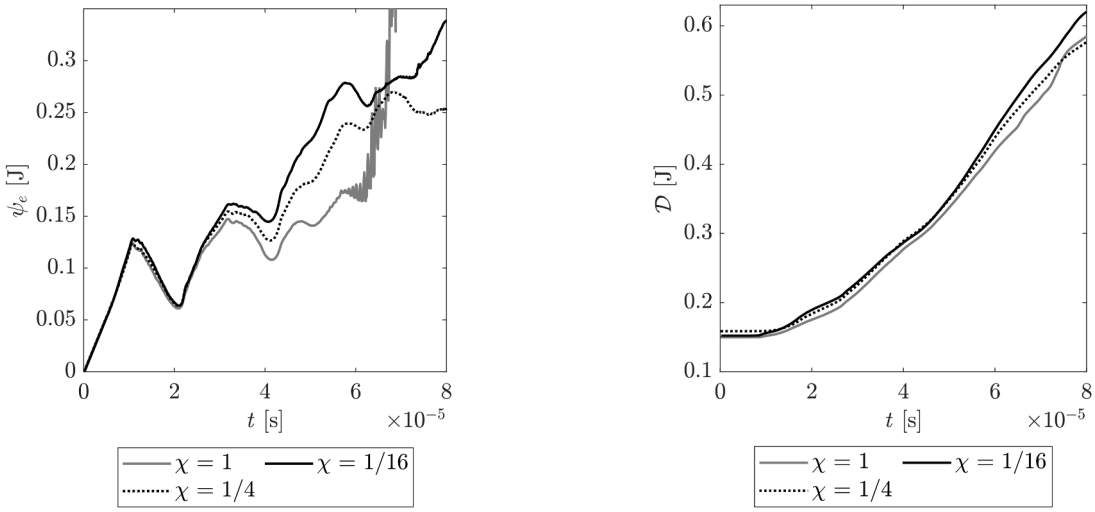

(a) Strain energy. (b) Dissipated energy.

Fig. 6. Dynamic crack branching test: strain energy (left) and dissipated energy (right) for$\Delta t = 10^{-7}$ s, mesh size $h = l_0/2$, and different values of χ, for the AT1 4th-order phase-field model.

explicitely computed as a function of χ. Moreover, for $\chi = 1$ (and actually also for larger values) the crack pattern exhibits a phase-field concentration[1] on the left hand side of the domain.

To further study the influence of χ, we focus on the strain and dissipated energies. Fig. 6(a) shows that considering $\chi = 1$ the strain energy becomes unstable. In contrast, reducing χ prevents the blow up of the internal energy curves.

The dissipated energy plots further confirm these results, as Fig. 6(b) illustrates that for $\chi = 1$ the curve's behavior is different compared to the response of the other curves.

Additionally, in Fig. 7 we report the crack length trends for different values of χ, computed with the image-based algorithm in [18], Appendix B. The crack length is in accordance with the strain and dissipated energy curves.

Thus, summarizing this first set of results, for $\Delta t = 10^{-7}$ s and $h = l_0/2$, the behavior of the energy curves turns out to be comparable for $\chi \leq 1/4$; therefore, we consider $(0, 1/4)$ as a reference interval for the parameter χ.

It is interesting to note that the parameter χ influences also the choice of the time step.

Fig. 8 shows in fact the effect of time-step size refinement for $h = l_0/2$ on the higher-order AT1 model for $\chi = 1$ and highlights that a slightly smaller value of Δt with respect to the choice typically recommended in the literature for AT2 (i.e., $\Delta t = 10^{-7}$ s) leads to the elimination of the nonphysical phase-field concentration (see Fig. 8(a)).

Further insights are provided studying the strain and dissipation energies for the 4th-order AT1 model. Namely, Fig. 9 shows that considering the literature reference time-step size for AT2, the strain energy becomes unstable while the dissipated energy is not accurate. These results indicate that for $\chi = 1$, Δt should be less than $8.5 \cdot 10^{-8}$ s. We believe that smaller values for the time step are needed since the Newmark scheme does not introduce numerical wave dumping. Therefore, having in mind both accuracy and computational time, the above results suggest to choose a small value of χ, for which larger time steps seem to provide accurate results.

[1] This behavior is aligned with what has been observed in the quasi-static case, where considering smaller displacement-based load increments eliminates the presence of the kink that forms in the SEN Shear test (we refer the interested reader to Section 8 of [7]).

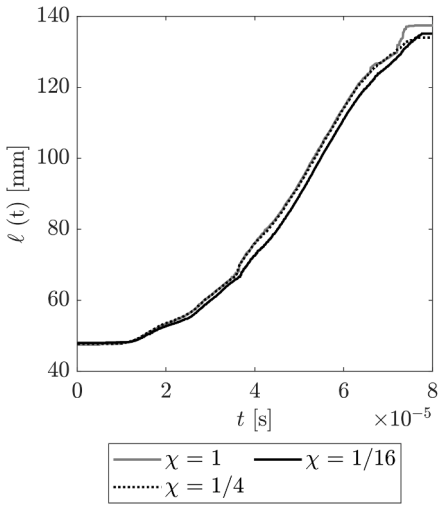

Fig. 7. Dynamic crack branching test: crack length for$\Delta t = 10^{-7}$s, mesh size $h = l_0/2$, and different values of χ, for the AT1 4th-order phase-field model.

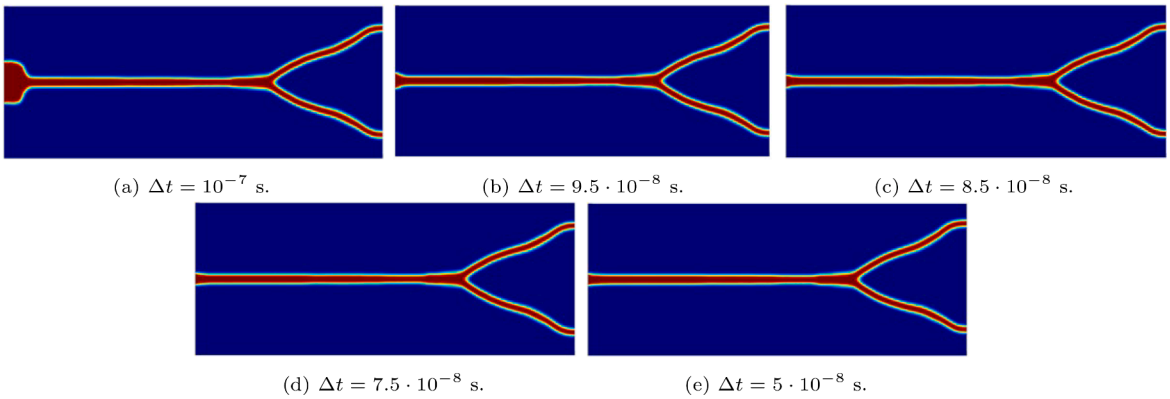

Fig. 8. Dynamic crack branching test: study of the influence of Δt for a fixed mesh size $h = l_0/2$ and $\chi = 1$. Crack pattern referred to $T = 80\ \mu s$.

4.3.2. Dynamic SEN shear test

In this section, we perform the previous parametric study for the 4th-order AT1 functional on the Dynamic SEN shear test. In Fig. 10 we can observe, for smaller values of χ, a reduction in the crack branching extent. Also, comparing the crack pattern obtained for the dynamic problem with the one in quasi-static (see, e.g., Section 4.3 of [18]), we highlight the presence of an additional crack in the dynamic case. However, it has been numerically verified that the secondary crack is generated by shear deformation only, as the strain tensor trace is positive at every time instant.

Additionally, the dissipated and strain energy curves shown in Fig. 11 confirm the behaviour highlighted in the previous subsection, even if instability is less pronounced. Furthermore, in Fig. 12 we compare the crack length, for different values of χ.

Even in this case, we can observe that lower values of χ correspond to a smaller fracture development. This result, consistent with what is shown in Fig. 10, leads us to conclude that: high values of χ cause a loss in the time-resolution and require smaller time-step sizes; in contrast, smaller values of χ allow to consider larger time-step sizes.

4.4. Comparison of 2nd- and 4th-order AT1 and AT2

In this section, we compare the 2nd- and 4th-order models, tested on the dynamic crack branching and SEN shear benchmarks. Following the idea of [7,18] we consider for the high-order models an element size twice as large as for the low-order counterparts. Unless otherwise specified, for the 4th-orders we consider a fixed mesh size $h = l_0/2$ and consequently a time step $\Delta t = 10^{-7}$ s, while the 2nd-orders a mesh size $h = l_0/4$ and time step $\Delta t = 5 \cdot 10^{-8}$ s. As discussed in the previous section, the 4th-order AT1 model introduces a weighting parameter χ in front of the higher-order regularization term and in all simulations presented herein, we adopt the value $\chi = 1/16$. With this choice, the AT1 regularization family yields a homogeneous physical response, as both the branching instants and the velocity curves are consistent and comparable, as it will be clear in the subsequent sections.

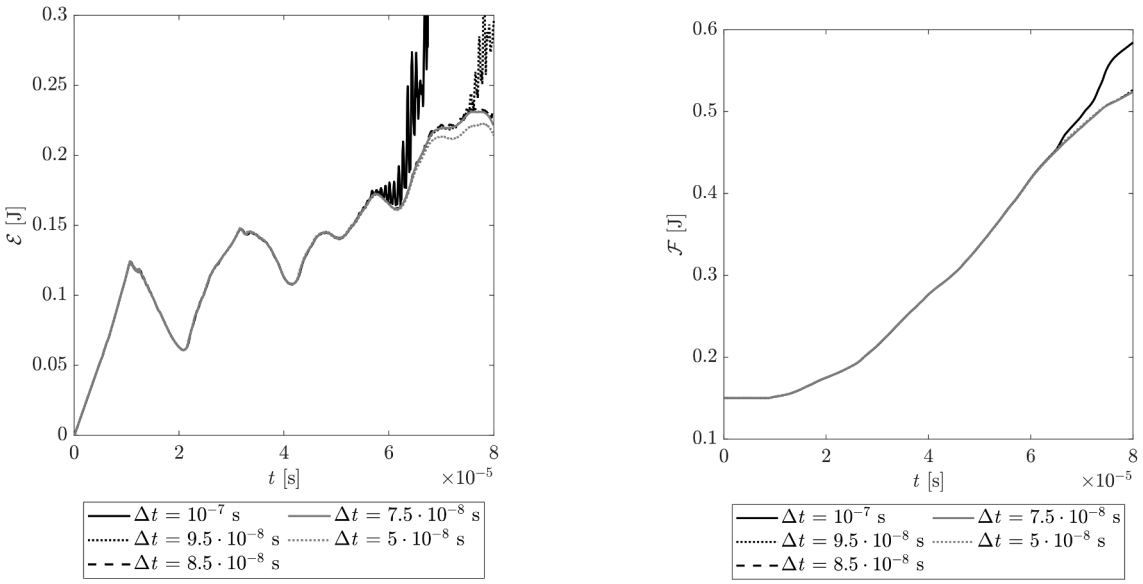

(a) Strain energy. (b) Dissipated energy.

Fig. 9. Dynamic crack branching test: strain energy (left) and dissipated energy (right) for a varying time-step size for the AT1 4th-order phase-field model with $\chi = 1$.

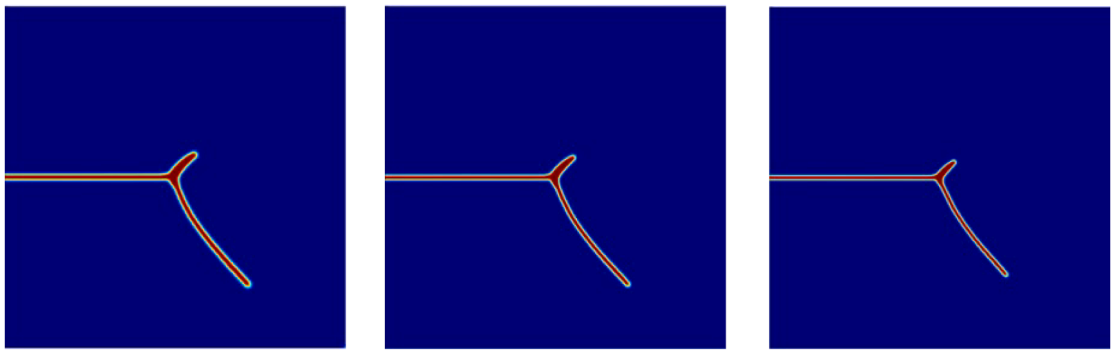

(a) $\chi = 1$. (b) $\chi = 1/4$. (c) $\chi = 1/16$.

Fig. 10. Dynamic SEN shear test: parametric study of the influence of the χ coefficient for fixed$\Delta t = 10^{-7}$ s and mesh size $h = l_0/2$.

4.4.1. *Crack pattern*

In Fig. 13, we first perform a qualitative comparison in terms of crack-patterns, analysing the dynamic crack branching sample for different mesh sizes.

It can be observed that for both the AT-models, the crack patterns of the 4th-order models obtained with a coarser mesh are qualitatively comparable with the 2nd-order ones. However, we highlight that the 4th-order branching point is slightly to the right of the 2nd-order one. Furthermore, the branches obtained with the 4th-order models and a coarser mesh exhibit a slightly lower opening angle.

In Fig. 14 we carry out the same comparison study for the dynamic SEN shear test. Also in this case, it is observed that the crack patterns of the AT1 models turn out to be qualitatively comparable considering for the 2nd-order model a mesh two times finer than the one utilized for the 4th-order formulation. For the AT2 model, the crack patterns are also comparable. However, in this case we report that the 4th-order crack pattern presents a less pronounced minor branch and an additional crack at the lower right corner, where the boundary condition is imposed. We also observe that the AT1 model propagates more than the corresponding AT2 counterparts and do not exhibit a diffuse damage away from the fracture propagation zone (as it is the case with the AT2 models).

4.4.2. *Wave propagation*

This section presents a comparative analysis of wave propagation for the different AT models, evaluated at three representative time instants. Additional snapshots, focusing on the 4th order AT1, are provided instead in Appendix D.

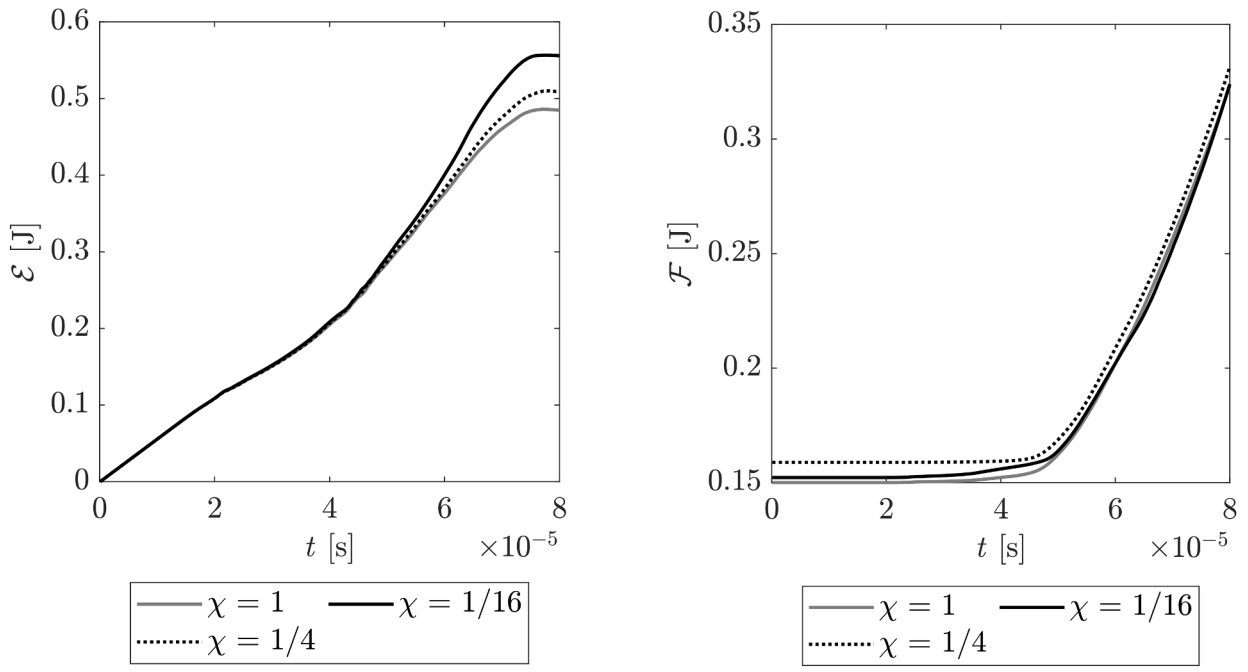

(a) Strain energy curves

(b) Dissipated energy curves

Fig. 11. Dynamic SEN shear test: strain energy (left) and dissipated energy (right) for $\Delta t = 10^{-7}$ s, mesh size $h = l_0/2$, and different values of χ, for the AT1 4th-order phase-field model.

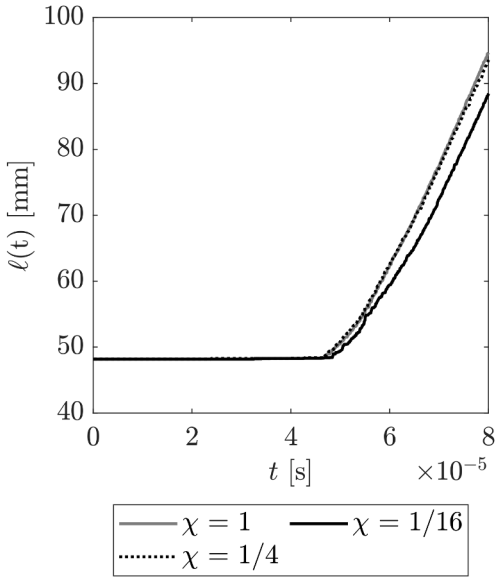

Fig. 12. Dynamic SEN shear test: crack length for different values of χ, for $\Delta t = 10^{-7}$ s, mesh size $h = l_0/2$, and different values of χ, for the AT1 4th-order phase-field model.

Fig. 15 shows the evolution of the P-waves using different spatial discretizations (and corresponding mesh-derived time-step sizes). As expected, the 2nd-order models exhibit sharper and more localized wavefronts compared to the 4th-order ones. Nevertheless, the overall propagation behavior remains comparable across all models, regardless of the adopted discretization.

Once fracture initiates, P-waves are emitted from the crack tip (see, e.g., Fig. 15(a)). At the onset of crack branching, additional waves with circular fronts emerge from the newly formed crack tips (see Fig. 15(b),(e),(h),(k)). These wavefronts continue to prop-

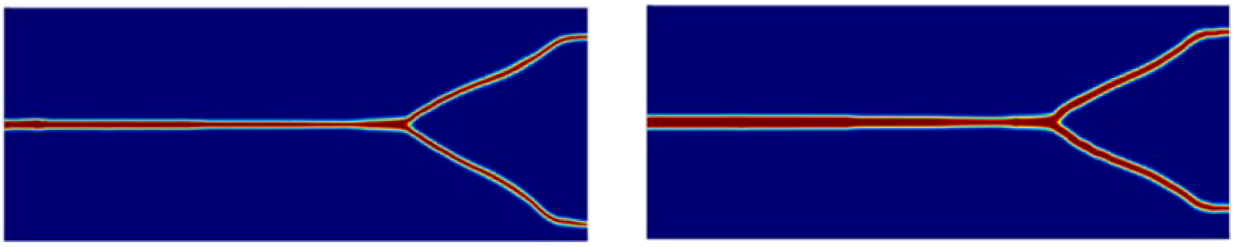

(a) 2nd-order AT1, h $= l_0/4$ and $\Delta t = 5 \cdot 10^{-8}$ s

(b) 4th-order AT1, h $= l_0/2$ and $\Delta t = 10^{-7}$ s

(c) 2nd-order AT2, h $= l_0/4$ and $\Delta t = 5 \cdot 10^{-8}$ s

(d) 4th-order AT2, h $= l_0/2$ and $\Delta t = 10^{-7}$ s

Fig. 13. Dynamic crack branching test: 2nd-vs 4th-order crack pattern comparison at time $T = 80\ \mu s$ for AT1 (top row) and AT2 models (bottom row) considering different meshes and time-step sizes.

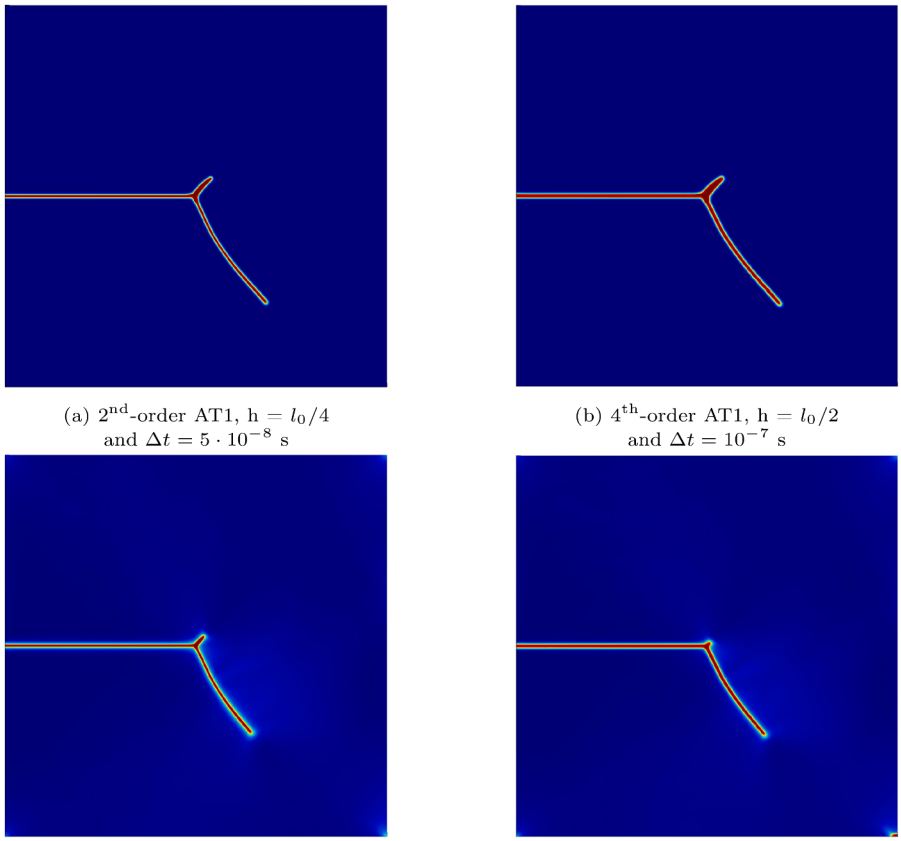

(a) 2nd-order AT1, h $= l_0/4$ and $\Delta t = 5 \cdot 10^{-8}$ s

(b) 4th-order AT1, h $= l_0/2$ and $\Delta t = 10^{-7}$ s

(c) 2nd-order AT2, h $= l_0/4$ and $\Delta t = 5 \cdot 10^{-8}$ s

(d) 4th-order AT2, h $= l_0/2$ and $\Delta t = 10^{-7}$ s

Fig. 14. Dynamic SEN Shear test: 2nd-vs 4th-order crack pattern comparison at time T $= 80\ \mu s$ for AT1 (top row) and AT2 models (bottom row) considering different meshes and time-step sizes.

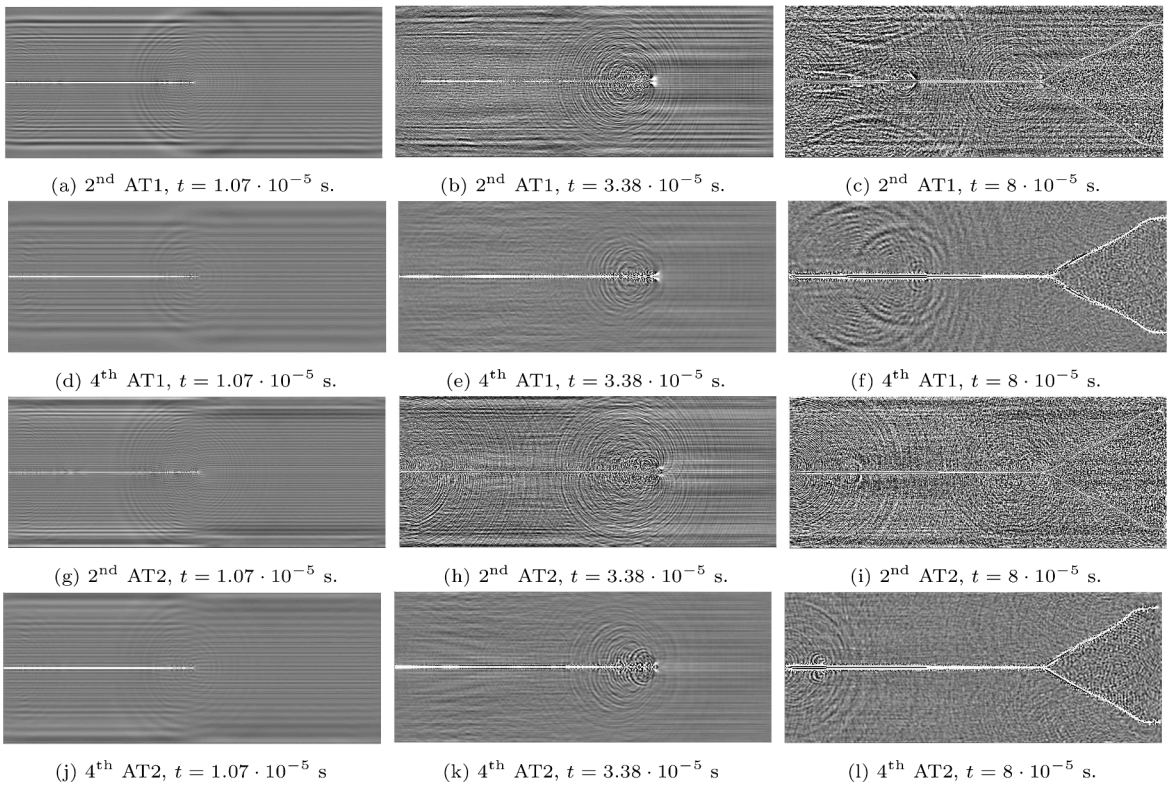

Fig. 15. Dynamic crack branching test: P-wave comparison for different phase-field models.

agate throughout the fractured domain and superimpose, resulting in increased background noise in the representation (see, e.g., Fig. 15(c)).

As for the P-wave, Fig. 16 presents a comparison of S-wave propagation for the different mesh size h and time-step size Δt. Overall, the wave behavior appears consistent across all models. Unlike the dynamic crack branching test discussed earlier, where variations in time-step size lead to differences in wavefront resolution, here all models exhibit comparable wavefront sharpness due to the uniform time integration parameters. As a result, the choice of the fracture model does not significantly influence S-wave propagation, and both 2nd- and 4th-order formulations yield similar results across different spatial discretizations.

4.4.3. Crack length and velocity of total crack growth

In this section, we quantitatively compare the crack patterns provided by the 2nd- and 4th-order AT models in terms of crack length and velocity of total crack growth. Specifically, the crack length is measured at each time instant by means of the imaging algorithm presented in [18], that is able to track complex fracture patterns. Instead, we compute the velocity of total crack growth at every time instant as:

$$v(t) = \frac{\ell_{n+1} - \ell_n}{\Delta t}, \tag{32}$$

where ℓ_n and ℓ_{n+1} denote the crack length of two subsequent time instants.

Fig. 17 compares the crack length and velocity of total crack growth for the 2nd- and 4th-order AT models, analyzing the dynamic crack branching test.

In all the results, we consider for the 4th-order model a mesh size two-times larger than for the 2nd-order one. We can observe that, fixing the regularization model (AT1 or AT2), the 2nd- and 4th-order formulations provide a virtually indistinguishable crack length. The fact that the two models, 2nd- and 4th-order exhibit the same behavior in terms of propagation velocity and fracture length (for a fixed AT1 or AT2 regularization) results in equal propagation time instants and branching time. More precisely, the 4th-order AT1 model bifurcates around 36 μs, exactly as the 2nd-order AT1 model. Instead, for the 4th-order AT2 model the bifurcation occurs at 37 μs and is again comparable with the behavior of the 2nd-order model.

Fig. 18 shows the comparison between 2nd- and 4th-order models in terms of crack length and velocity of total crack growth for AT1 (Fig. 18(a)) and AT2 (Fig. 18(b)) models in the dynamic SEN shear test case. We can observe that also for this benchmark, fixing the regularization model (either AT1 or AT2), the 2nd- and 4th-order models show a comparable crack length. While in the AT1 case the curves are virtually indistinguishable, for AT2 we highlight a mild discrepancy between low- and high-order curves due to the presence of a less pronounced secondary branch in the 4th-order example. Again, for what concerns the velocity of total crack growth,

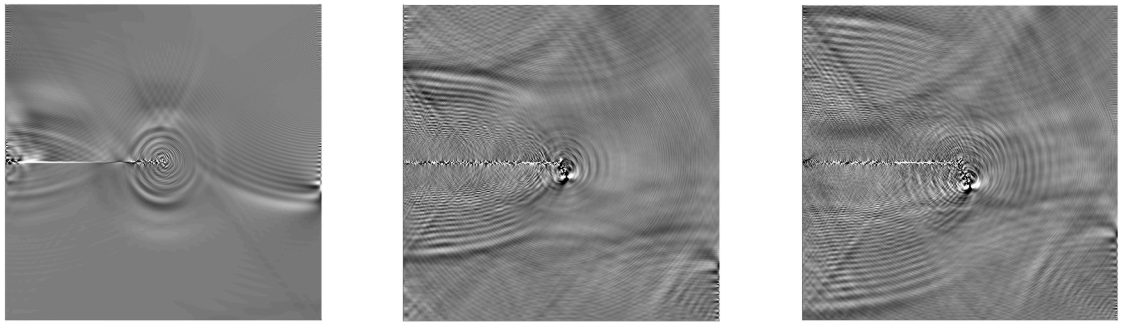

(a) 2nd AT1, $t = 2.47 \cdot 10^{-5}$ s. (b) 2nd AT1, $t = 5.14 \cdot 10^{-5}$ s. (c) 2nd AT1, $t = 5.75 \cdot 10^{-5}$ s.

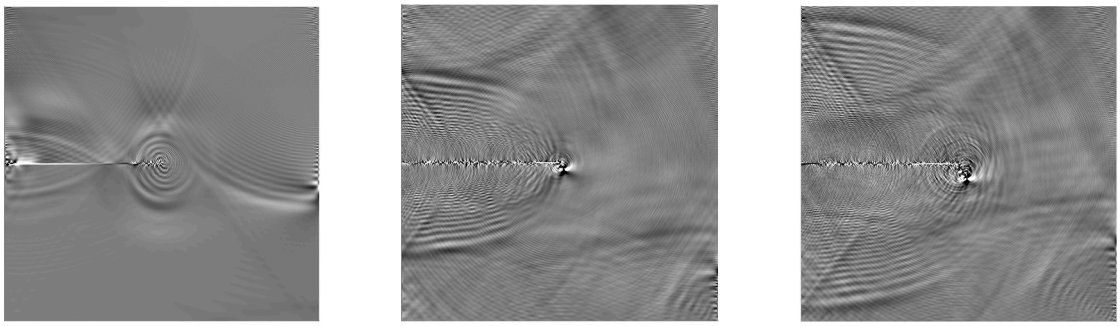

(d) 2nd AT2, $t = 2.47 \cdot 10^{-5}$ s. (e) 2nd AT2, $t = 5.14 \cdot 10^{-5}$ s. (f) 2nd AT2, $t = 5.75 \cdot 10^{-5}$ s.



(g) 4th AT1, $t = 2.47 \cdot 10^{-5}$ s. (h) 4th AT1, $t = 5.14 \cdot 10^{-5}$ s. (i) 4th AT1, $t = 5.75 \cdot 10^{-5}$ s.

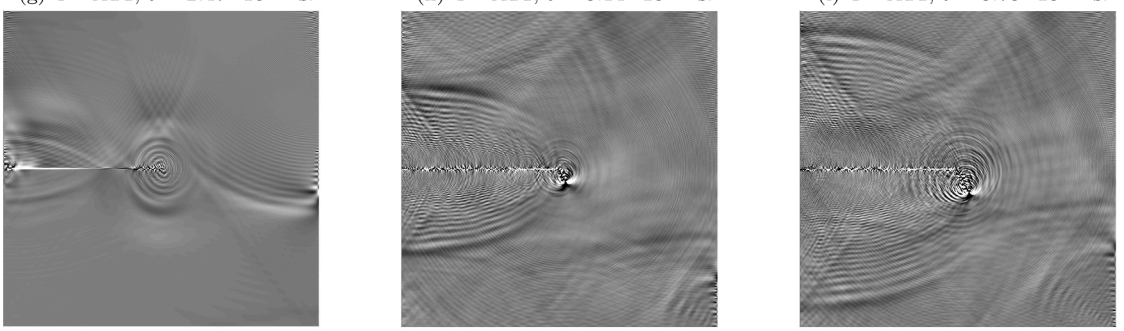

(j) 4th AT2, $t = 2.47 \cdot 10^{-5}$ s. (k) 4th AT2, $t = 5.14 \cdot 10^{-5}$ s. (l) 4th AT2, $t = 5.75 \cdot 10^{-5}$ s.

Fig. 16. Dynamic SEN shear test: comparison of relevant S-wave propagation instants for different phase-field models.

we observe that the AT1 models propagate faster than the AT2 ones. Additionally, also in this case fixing the regularization family, the 2nd- and 4th-order models propagate at the same velocity.

Remark 2. The high number of steps in the analysis does not make a clear representation of velocity of total crack growth possible. For this reason, the velocity shown in Figs. 17 and 18 is the result of a filtering operation, by means of the `MATLAB` filter function called "`lowess filter`", which allows us to observe the trend of the curve, while eliminating the background noise.

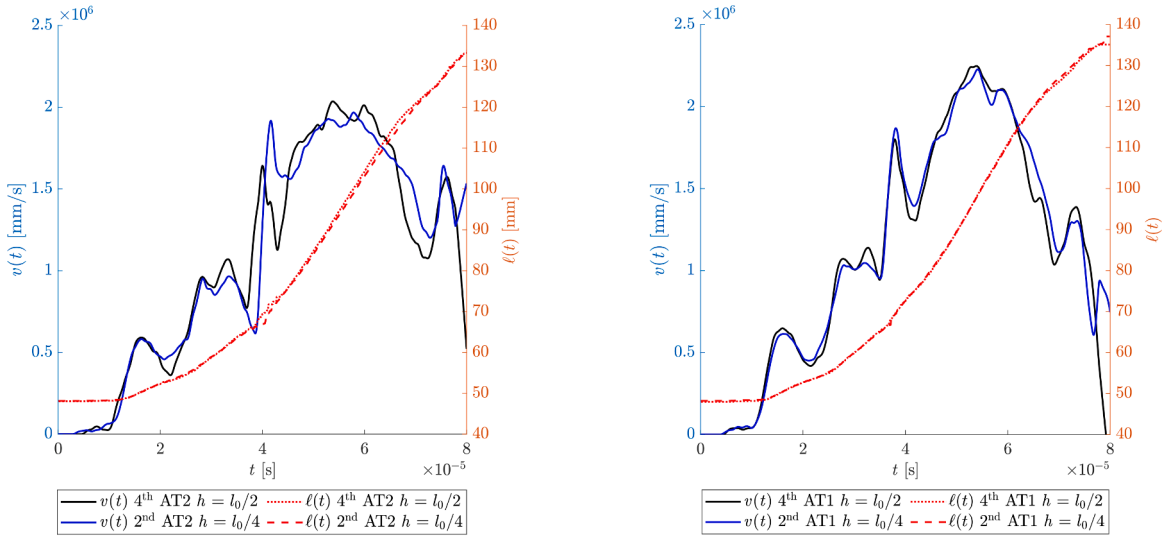

(a) 2nd- *vs* 4th-order AT2 (b) 2nd- *vs* 4th-order AT1

Fig. 17. Dynamic crack branching test: 2nd-vs 4th-order crack length and velocity of total crack growth comparison in time for different meshes.

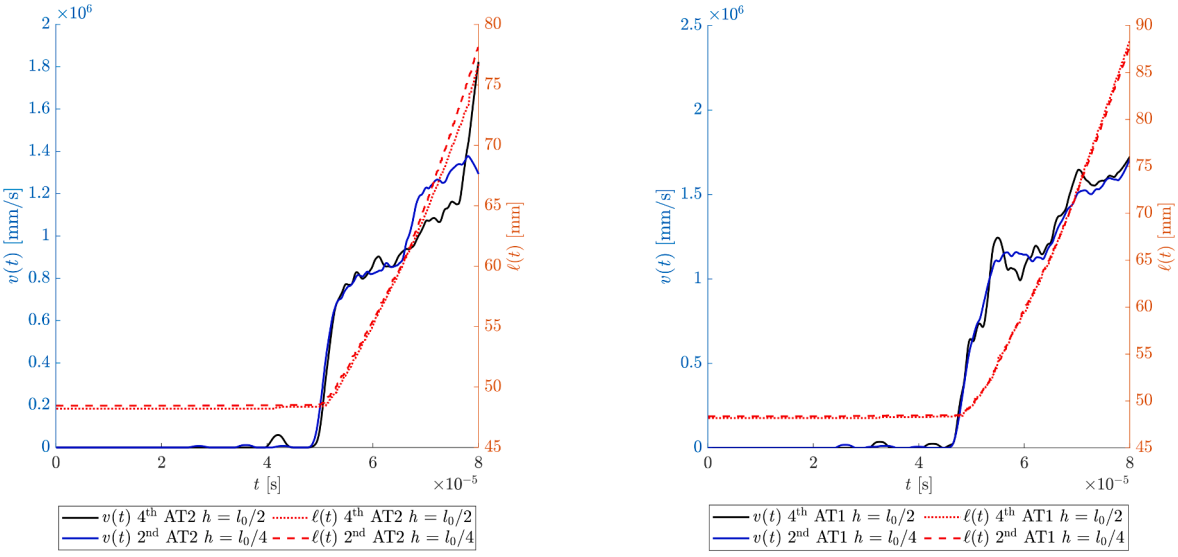

(a) 2nd- *vs* 4th-order AT2 (b) 2nd- *vs* 4th-order AT1

Fig. 18. Dynamic SEN Shear test: 2nd-vs 4th-order crack length and velocity of total crack growth comparison in time for different meshes.

Regarding the computational cost, we highlight that the use of high-order models leads to significant computational advantage, and they allow to obtain comparable results to their low-order counterparts using a coarser mesh size. This translates into the possibility to advance in time with a larger time-step size, given its dependence on the mesh size [8]. This turns to an estimate of 90 % in terms of computational time savings (approximately 20 % gain with respect to the static case [7,18]). The computational time required for an overall analysis[2] is summarized in Table 2.

4.5. Pure traction test

In quasi-static phase-field fracture, the elastic limit in 1D is computed under the hypothesis of uniform stress in the body. Clearly, this assumption is not valid in dynamics; however, the computations leading to the stress threshold still hold. Indeed, the quasi-static

[2] The simulations are performed on an HPC cluster, without parallelization, on one node having RAM = 256 GB.

Table 2
Computational time for the considered implicit dynamic tests.

Model	Mesh size [mm]	Dynamic crack branching [dd:hh]	Dynamic SEN shear [dd:hh]
2nd-order AT1	$l_0/4$	3:12	26:19
4th-order AT1	$l_0/2$	0:08	1:10
2nd-order AT2	$l_0/4$	3:19	29:12
4th-order AT2	$l_0/2$	0:11	1:12

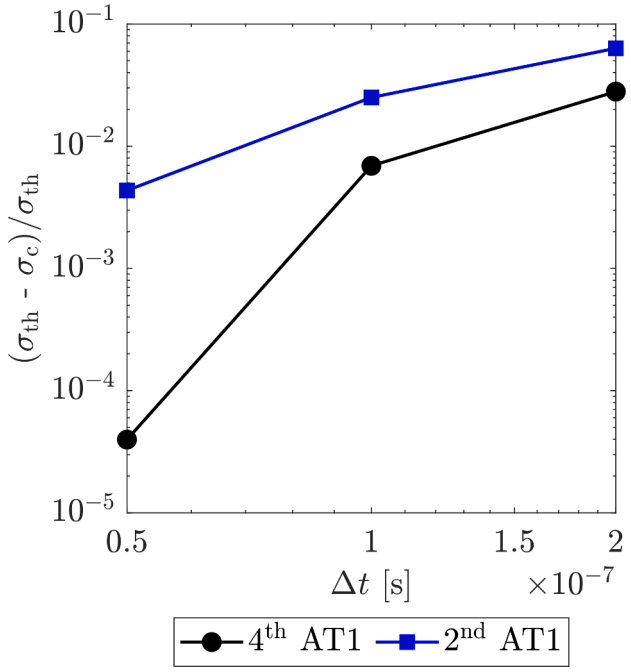

Fig. 19. Dynamic pure traction test: convergence in time for fixed mesh size $h = l_0/2$.

1D calculations are equivalent to the local (or pointwise) variation with respect to the damage parameter d of the elastic energy density $\psi_e(\epsilon, d)$ and the low order part of the fracture energy $d/c_\chi l_0$. This argument is still valid in dynamics since, in the staggered scheme, damage is updated minimizing the energy with respect to d keeping displacement $\mathbf{u}$ and velocity $\dot{\mathbf{u}}$ fixed. As a result, in our dynamic setting we expect the same stress threshold of the quasi-static setting, i.e.

$$\sigma_{\text{th}} = \sqrt{\frac{2G_c\mu}{c_\chi l_0}}. \tag{33}$$

Note that in Eq. (33), σ_{th} is computed as a function of the material toughness G_c, shear modulus μ, internal length l_0, and normalization constant c_χ (or c_α for the 2nd-order AT1 model in Eq. $(6)_2$). The normalization constants change according to the adopted model: for example, $c_\alpha = 8/3$ for the 2nd-order AT1 formulation while $c_\chi = 3.1615$ in the 4th-order AT1 model case with $\chi = 1/16$ (for more details on the regularization constants we refer the interested reader to §6 and §7 of [7]). In this framework, the theoretical elastic limit for the 2nd-order model is $\sigma_{\text{th}} = 2.7586\,\text{N/mm}^2$ and for the 4th-order one is $\sigma_{\text{th}} = 2.5152\,\text{N/mm}^2$.

Thus, we consider the pure traction test, without any initial crack, as described in Section 4.1 and study the trend of the stress threshold as the time-step size varies for a fixed mesh ($h = l_0/2$).

In Fig. 19, specifically for the 4th-order model, we observe very small relative errors, in the order of those obtained in the quasi-static case in [7], whereas the convergence speed is faster than the 2nd-order one. This behavior may be related to the mesh size choice, which might not be fine enough for the 2nd-order model. It is interesting to note that the 4th-order model shows comparable relative errors to the 2nd-order one, even though considering time-step sizes twice as large. The results in terms of relative errors are also summarized in Table 3.

Additionally, Fig. 20 shows the dynamic crack patterns. We can observe that, for both 2nd- and 4th-order models, the fracture always forms in the center of the specimen, unlike in the quasi-static case.

Thus, we turn our attention to the influence of wave propagation on the development of fracture, focusing on the 4th-order AT1 model and report in Fig. 21 the behavior of the P-waves for this test. Unlike previous benchmarks, the initial configuration of the pure traction test does not feature an initial pre-crack. As a result, wave propagation begins in an initially undamaged continuum,

Table 3
Dynamic pure traction test: elastic limit relative error trends.

Δt [s]	2nd AT1 [%]	4th AT1 [%]
$2 \cdot 10^{-7}$	4.502	2.799
$1 \cdot 10^{-7}$	2.508	0.692
$5 \cdot 10^{-8}$	0.435	0.004



(a) 2nd-order AT1 model

(b) 4th-order AT1 model

Fig. 20. Dynamic pure traction test: 2nd- and 4th-order crack patterns.

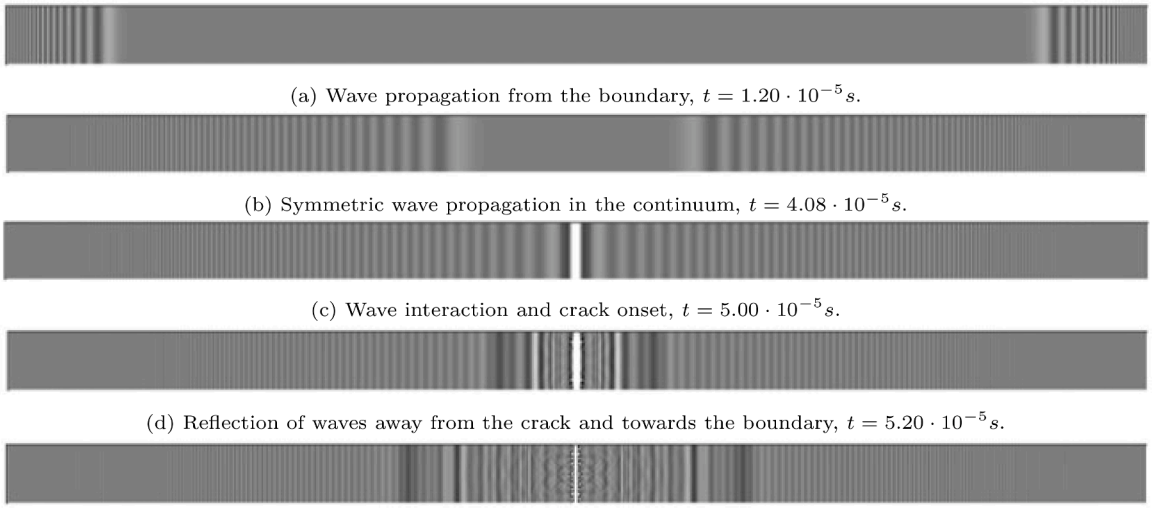

(a) Wave propagation from the boundary, $t = 1.20 \cdot 10^{-5} s$.

(b) Symmetric wave propagation in the continuum, $t = 4.08 \cdot 10^{-5} s$.

(c) Wave interaction and crack onset, $t = 5.00 \cdot 10^{-5} s$.

(d) Reflection of waves away from the crack and towards the boundary, $t = 5.20 \cdot 10^{-5} s$.

(e) Overlap between reflected waves and load-generated waves, $t = 7.34 \cdot 10^{-5} s$.

Fig. 21. Propagation of P-waves in the pure tensile test using the 4th-order AT1 model.

originating symmetrically from the domain boundaries due to the applied boundary conditions (see Fig. 21(a)–(b)). When the waves meet at the center of the specimen, a crack forms, as shown in Fig. 21(c). From that instant onward, the domain behaves as two separate bodies and the reflected waves from the crack interface interact with those generated by the boundary loading.

5. Conclusion

This work presents a comprehensive numerical investigation of dynamic brittle fracture within the phase-field framework, addressing both accuracy and computational performance. A semi-implicit staggered scheme, coupling the Newmark method with the Projected Successive Over-Relaxation algorithm, showcases to accurately solve the coupled elastodynamic and phase-field problems. The Newmark method, in particular, avoids artificial numerical dissipation and ensures energy conservation, thereby providing an accurate representation of P- and S-wave propagation and their interaction with the evolving cracks.

Thus, we focus on the 4th-order AT1 model and provide a detailed parametric study that highlights the role of the coefficient χ, weighting the higher-order regularization term, and its connection with the time step Δt. Smaller values of χ slightly reduce the length of the crack but avoid the blowup of the elastic energy, while refined time-steps mitigate spurious localizations observed under standard time-step computation rules. These results emphasize the need to jointly tune χ and Δt to balance accuracy and computational cost. Additionally, the analysis of the elastic limit further confirms that the 4th-order AT1 model converges more rapidly to the analytical threshold compared to its 2nd-order counterpart, underscoring its advantages in dynamic settings. Finally, comparing the 4th-order AT1 formulation to reference 2nd- and 4th-order phase-field models in the literature showcases that the

former can reproduce equivalent fracture patterns, propagation rates, and wave behavior with substantially coarser meshes and larger time-steps, yielding significant computational savings without compromising the quality of the results.

Future work will explore alternative energy decomposition strategies, explicit dynamics, and shell formulations, as well as the integration of high-order models into open-source isogeometric libraries to enhance their accessibility for large-scale engineering applications.

CRediT authorship contribution statement

L. Greco: Conceptualization, Methodology, Software, Validation, Formal analysis, Investigation, Writing – original draft, Visualization; **J. Kiendl:** Conceptualization, Methodology, Writing – review & editing, Visualization, Funding acquisition; **M. Negri:** Conceptualization, Methodology, Validation, Formal analysis, Investigation, Writing – original draft, Visualization; **A. Patton:** Conceptualization, Methodology, Validation, Formal analysis, Investigation, Writing – original draft, Visualization; **A. Reali:** Conceptualization, Methodology, Writing – review & editing, Visualization, Funding acquisition.

Data availability

The data that support the findings of this study are avaiable from the authors upon reasonable request.

Declaration of competing interest

I, Luigi Greco, on behalf of all co-authors, hereby declare that our manuscript titled “Fourth-order isogeometric phase-field modeling of dynamic brittle fracture: Numerical study and comparison with second-order models” is not currently submitted to other journals. Furthermore, we confirm that it will not be submitted to any other journals during the review process.

Acknowledgements

L. Greco gratefully acknowledges the “Erasmus + Traineeship 2023/24” and “Bando di mobilita’ internazionale - 15a edizione” programmes, that partially supported him within the collaboration between the University of Pavia and the Universität der Bundeswehr München.

A. Reali is a member of the Gruppo Nazionale Calcolo Scientifico-Istituto Nazionale di Alta Matematica (GNCS-INDAM), and acknowledges the support of the Italian Ministry of University and Research (MUR) through the PRIN project COSMIC (No. 2022A79M75), funded by the European Union - Next Generation EU, as well as the contribution of the National Recovery and Resilience Plan, Mission 4 Component 2 - Investment 1.4 - NATIONAL CENTER FOR HPC, BIG DATA AND QUANTUM COMPUTING, spoke 6.

M. Negri is a member of GNAMPA - INdAM and was supported by PRIN 2022 (Project no. 2022J4FYNJ), funded by MUR, Italy, and the European Union - Next Generation EU, Mission 4 Component 1 CUP F53D23002760006.

A. Patton was supported by the European Research Council through the H2020 ERC Consolidator Grant 2019 n. 864,482 FDM2.

J. Kiendl partially supported by the European Research Council through the H2020 ERC Consolidator Grant 2019 n. 864,482 FDM2.

Appendix A. Integral representation of the variational formulation

We further detail Euler-Lagrange equations in integral form (13), obtaining

$$\frac{\mathrm{d}}{\mathrm{d}t}\Big(\frac{\partial \mathcal{K}}{\partial \dot{\mathbf{u}}}\big(\dot{\mathbf{u}}(t)\big)\Big)[\delta\mathbf{u}] = \int_\Omega \rho\,\ddot{\mathbf{u}}(t)\cdot\delta\mathbf{u}\,\mathrm{d}\Omega, \tag{A.1}$$

$$\begin{aligned}\frac{\partial \Psi}{\partial \mathbf{u}}\big(\mathbf{u}(t),d(t)\big)[\delta\mathbf{u}] &= \int_\Omega \boldsymbol{\sigma}(\mathbf{u}(t),d(t)) : \boldsymbol{\varepsilon}(\delta\mathbf{u})\,\mathrm{d}\Omega - \int_{\partial_N\Omega}\mathbf{f}(t)\cdot\delta\mathbf{u}\,\mathrm{d}(\partial\Omega_N)\\ &= -\int_\Omega \mathrm{div}\big(\boldsymbol{\sigma}(\mathbf{u}(t),d(t))\big)\cdot\delta\mathbf{u}\,\mathrm{d}\Omega + \int_{\partial_N\Omega}\big(\boldsymbol{\sigma}(\mathbf{u}(t),d(t))\,\boldsymbol{\nu}-\mathbf{f}(t)\big)\cdot\delta\mathbf{u}\,\mathrm{d}(\partial\Omega_N)\,.\end{aligned} \tag{A.2}$$

Then, for the Karush–Kuhn–Tucker conditions (14), it is necessary to distinguish between the 2nd- and 4th-order models. Specifically, in the former case we have

$$\frac{\partial \Psi}{\partial d}(\mathbf{u}(t),d(t))[\delta d] = \int_\Omega w'(d(t))\,\psi_e^+\big(\boldsymbol{\varepsilon}(\mathbf{u}(t))\big)\,\delta d\,\mathrm{d}\Omega + \frac{G_c}{c_\alpha l_0}\int_\Omega \alpha'(d(t))\,\delta d + 2l_0^2\,\nabla d(t)\cdot\nabla(\delta d)\,d\Omega, \tag{A.3}$$

whereas in the case of the fourth-order AT1 model we have

$$\begin{aligned}\frac{\partial \Psi}{\partial d}(\mathbf{u}(t),d(t))[\delta d] = &\int_\Omega w'(d(t))\,\psi_e^+\big(\boldsymbol{\varepsilon}(\mathbf{u}(t))\big)\,\delta d\,\mathrm{d}\Omega\\ &+ \frac{G_c}{c_\chi l_0}\int_\Omega \delta d(t) + 2l_0^2\,\nabla d(t)\cdot\nabla(\delta d) + 2\chi l_0^4\,\Delta d(t)\,\Delta(\delta d)\,d\Omega\,.\end{aligned} \tag{A.4}$$

Instead, for AT2, similar formulations hold in the 2nd- and 4th-order cases by utilizing different normalization parameters, as well as weighting coefficients in the surface energy functionals, and therefore we omit this redundant information.

Appendix B. Evolution in terms of PDEs

Taking into account the initial and Dirichlet boundary conditions, from (A.1) and (A.2) we obtain the classic elasto-dynamic system at time t (where the stress depends also on the phase-field d)

$$\begin{cases} \rho\ddot{\mathbf{u}}(t) = \operatorname{div}\big(\boldsymbol{\sigma}(\mathbf{u}(t), d(t))\big) & \text{in } \Omega, \\ \boldsymbol{\sigma}(\mathbf{u}(t), d(t))\,\boldsymbol{\nu} = \mathbf{f}(t) & \text{in } \partial\Omega_N, \\ \mathbf{u}(t) = \mathbf{g}(t) & \text{in } \partial\Omega_D, \\ \mathbf{u}(0) = \mathbf{u}_0,\ \dot{\mathbf{u}}(0) = \dot{\mathbf{u}}_0 & \text{in } \Omega\,. \end{cases} \tag{B.1}$$

Instead, recasting (14) in terms of PDEs is more delicate (see [26] for further details) and, for 2nd-order functionals, by (A.3) we have

$$\begin{cases} G_c\big(\alpha'(d(t)) - 2l_0^2\Delta d(t)\big) + c_\alpha l_0\, w'(d)\,\psi_e^+\big(\boldsymbol{\varepsilon}(\mathbf{u}(t))\big) \geq 0 & \text{in } \Omega, \\ \big[G_c\big(\alpha'(d(t)) - 2l_0^2\Delta d(t)\big) + c_\alpha l_0\, w'(d)\,\psi_e^+\big(\boldsymbol{\varepsilon}(\mathbf{u}(t))\big)\big]\dot{d}(t) = 0 & \text{in } \Omega, \\ \nabla d(t)\cdot\boldsymbol{\nu} \geq 0 & \text{in } \partial\Omega, \\ [\nabla d(t)\cdot\boldsymbol{\nu}]\,\dot{d}(t) = 0 & \text{in } \partial\Omega, \end{cases} \tag{B.2}$$

whereas for 4th-order AT1 functionals, using Eq. (A.4) we get the following system

$$\begin{cases} G_c\big(1 - 2l_0^2\Delta d(t) + 2\chi l_0^4\Delta^2 d(t)\big) + c_\chi l_0\, w'(d)\,\psi_e^+\big(\boldsymbol{\varepsilon}(\mathbf{u}(t))\big) \geq 0 & \text{in } \Omega, \\ \big[G_c\big(1 - 2l_0^2\Delta d(t) + 2\chi l_0^4\Delta^2 d(t)\big) + c_\chi l_0\, w'(d)\,\psi_e^+\big(\boldsymbol{\varepsilon}(\mathbf{u}(t))\big)\big]\dot{d}(t) = 0 & \text{in } \Omega, \\ \nabla\big(d(t) - \chi l_0^2\Delta d(t)\big)\cdot\boldsymbol{\nu} \geq 0 & \text{in } \partial\Omega, \\ \big[\nabla\big(d(t) - \chi l_0^2\Delta d(t)\big)\cdot\boldsymbol{\nu}\big]\,\dot{d}(t) = 0 & \text{in } \partial\Omega\,. \end{cases} \tag{B.3}$$

As the procedure is similar to the AT1 case, to avoid redundancy we omit the derivations for the AT2 model.

Appendix C. Numerical evaluation of the principle of energy conservation and Griffith's criterion in dynamics

In this Appendix, we numerically verify the principle of energy conservation, employed in (12) to derive the evolution equations, i.e.,

$$\frac{\mathrm{d}}{\mathrm{d}t}\Big(\mathcal{K}(\dot{\mathbf{u}}(t)) + \mathcal{E}(\mathbf{u}(t), d(t)) - \mathcal{W}^{\text{ext}}(\mathbf{u}(t), t) + G_c\mathcal{F}(d(t))\Big) = 0, \tag{C.1}$$

that will be assessed in its in integral form, namely

$$\mathcal{K}(\dot{\mathbf{u}}(t_n)) + \mathcal{E}(\mathbf{u}(t_n), d(t_n)) + G_c\mathcal{F}(d(t_n)) = \mathcal{K}(\dot{\mathbf{u}}(t_0)) + \mathcal{E}(\mathbf{u}(t_n), d(t_0)) + G_c\mathcal{F}(d(t_0)) + \mathcal{W}^{\text{ext}}(\mathbf{u}(t_n), t_n)\,. \tag{C.2}$$

In Fig. C.22 we report in blue the left-hand side of Eq. (C.2), whereas in black its right-hand side. This study considers again the Dynamic Crack Branching test, whose geometry and boundary conditions are shown in Fig. 1, while its material and loading data are summarized in Table 1. The simulations are carried out using a mesh size and time step respectively of $h = l_0/4$ and $\Delta t = 5\cdot 10^{-8}$ s for the low-order models, whereas $h = l_0/2$ and $\Delta t = 10^{-7}$ s for the high-order ones. In Fig. C.22 we can observe that the AT2 models, in particular the 4th-order AT2 formulation, seem to better satisfy identity (C.2) with respect to the AT1 ones, whereas the high-order models exhibit an improved behavior in comparison to the low-order counterparts.

We remark that the fulfillment of the conservation of energy (C.2) indirectly implies Griffith's criterion [1] in dynamics and, therefore, we can rewrite (C.1) as

$$\frac{\mathrm{d}}{\mathrm{d}\ell}\Big(\mathcal{K}(\dot{\mathbf{u}}(t)) + \mathcal{E}(\mathbf{u}(t), d(t)) - \mathcal{W}^{\text{ext}}(\mathbf{u}(t), t) + G_c\mathcal{F}(d(t))\Big)\frac{\mathrm{d}\ell}{\mathrm{d}t} = 0, \tag{C.3}$$

where a denotes the crack length. In order to verify Eq. (C.3), we compute the time-discrete variation of the energies with respect to the time-discrete variation of the crack length, which is evaluated with the imaging algorithm proposed in [18].

In Fig. C.23, describing the discretized counterpart of Eq. (C.1), it can be observed that the response of the 4th-order models is closer to zero with respect to the 2nd-order ones, highlighting that the 4th-order formulation meets Griffith's criterion even in the dynamic case and with smaller deviations with respect to the 2nd-order models. Re markably, the 4th-order AT2 formulation exhibits almost negligible fluctuations with respect to all other models.

Remark 3. We remark that the plots in Figs. C.22,C.23(c)-(d) correspond to two 4th-order models, each characterized by a different set of coefficients within the energy dissipation functional (Eqs. (8)-(9)). For the AT2 4th-order model, the coefficients (1 - 1/2 - 1/16) are used, while for the AT1 4th-order model, the coefficients (1 - 1 - 1/16) are adopted. For an in-depth analysis of the selection of coefficients within the energy dissipation functional, the interested reader is referred to [7].

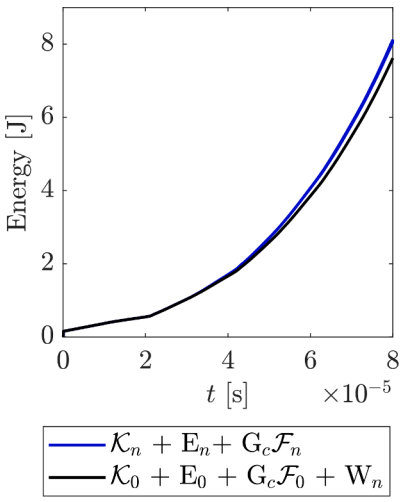

(a) 2nd order AT1

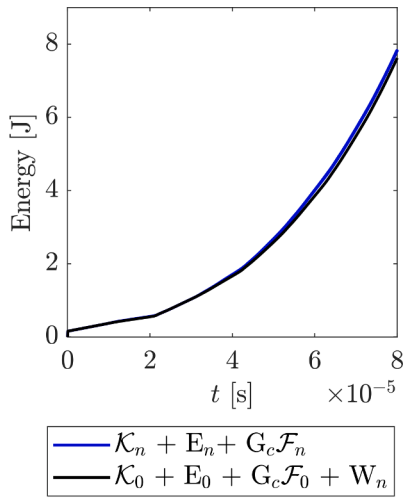

(b) 2nd order AT2

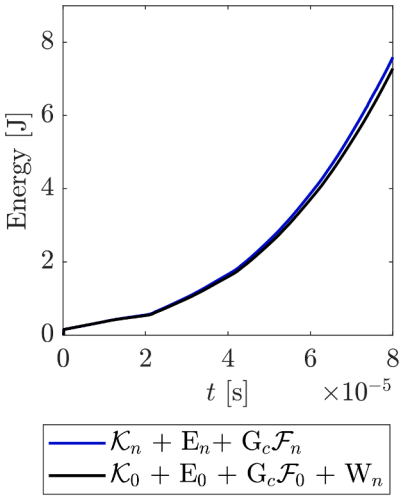

(c) 4th order AT1

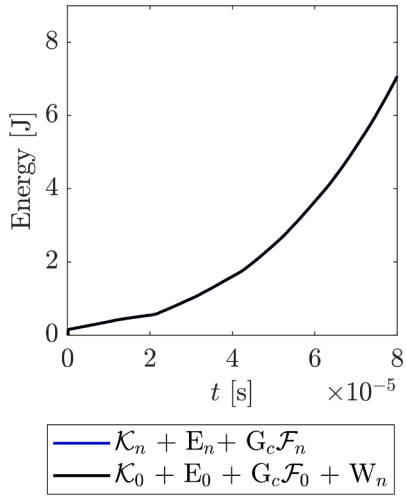

(d) 4th order AT2

Fig. C.22. Dynamic crack branching test: representation of the principle of energy conservation (Eq. (C.2)).

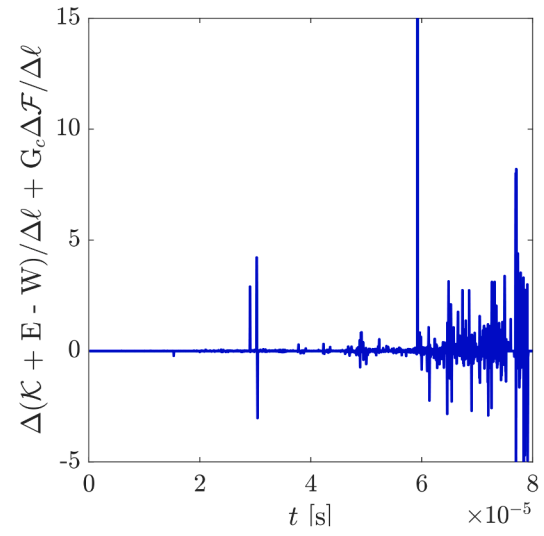

(a) 2nd order AT1

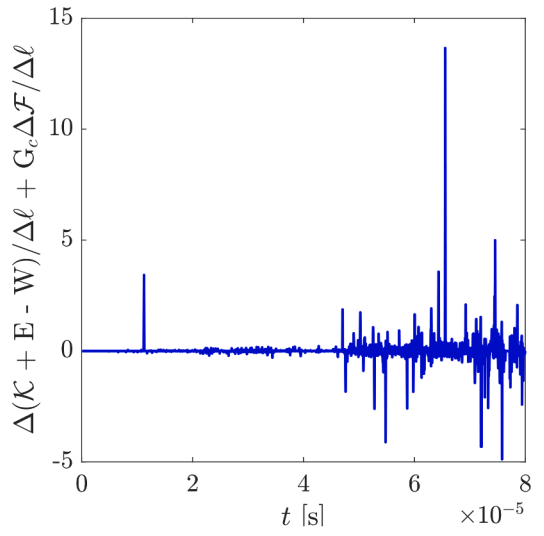

(b) 2nd order AT2

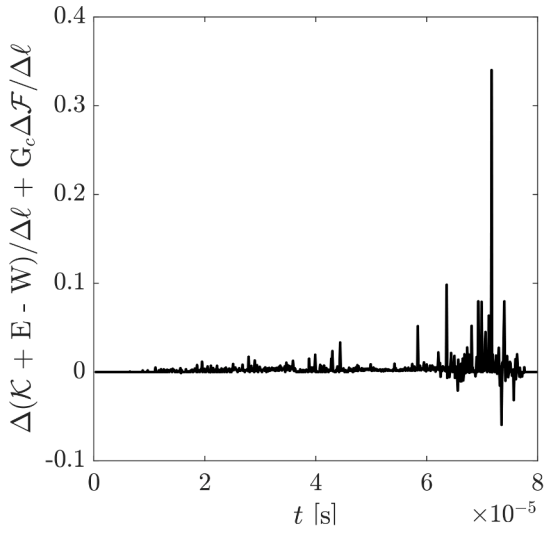

(c) 4th order AT1

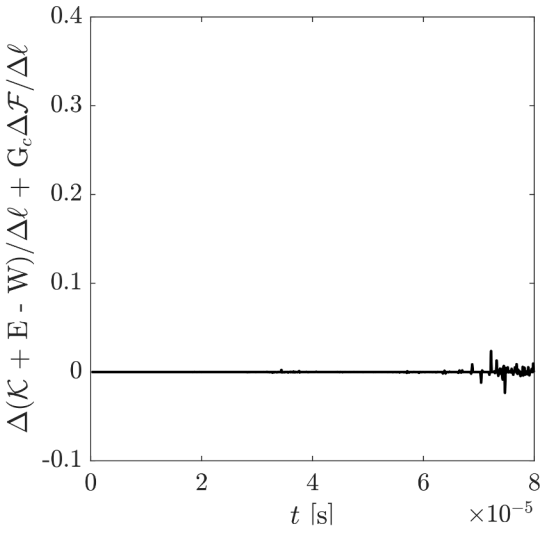

(d) 4th order AT2

Fig. C.23. Dynamic crack branching test: implicit Griffith's criterion evaluation at each instant of time.

Appendix D. Wave propagation in fractured domain

In this appendix, we first consider the dynamic crack branching test, modeled *via* the 4th order AT1 regularization and focus on how the P-wave propagation influences the crack onset.

Fig. D.24(a) illustrates the initial instant of the simulation. Subsequently, Fig. D.24(b) captures the onset of wave propagation from the loaded edges, with the waves traveling until they encounter the pre-existing crack (Fig. D.24(c)). Notably, the fracture acts as a free surface, reflecting waves back towards the specimen upper and lower edges. When fracture propagation initiates (Fig. D.24(d)), changes in the displacement and velocity fields become evident, leading to the generation of P-waves at the crack tip. These newly formed waves superimpose with the waves reflected from the fracture towards the boundaries, modifying the overall wavefront shape.

In Fig. D.24(e), the wave generated at the crack tip is shown scattering off the boundary. Simultaneously, the wave that had previously bounced off the boundary is observed returning towards the crack tip, further altering the wave pattern. Fig. D.24(f)

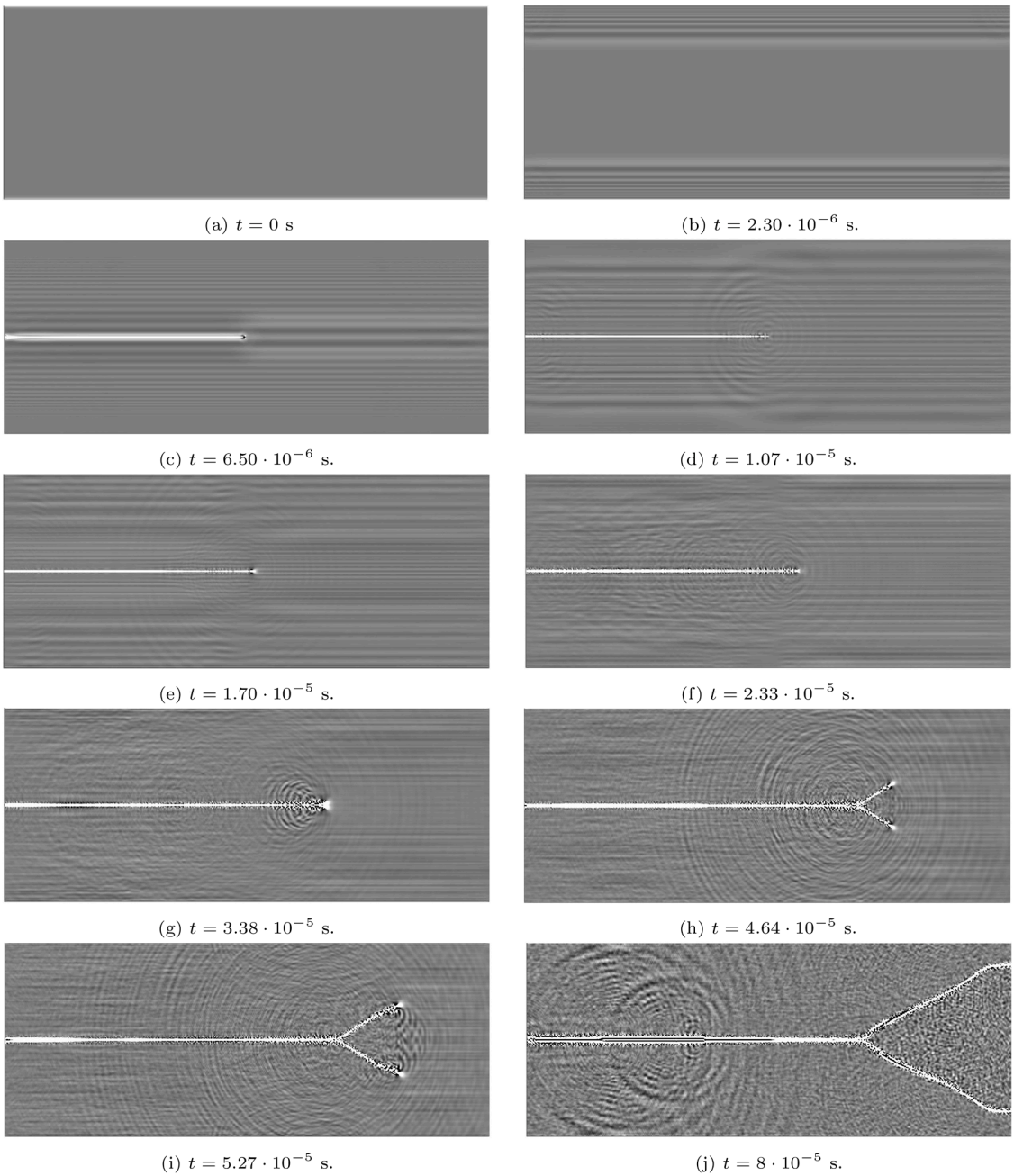

Fig. D.24. Dynamic crack branching test: Relevant P-wave propagation instants in the fractured continuum for the 4th-order AT1 model.

depicts the waves returning to the crack and undergoing additional reflection. This accumulation of waves results from hemispherical waves reflecting from the crack and combining with those propagating towards the domain edges.

As fracture propagation continues, a concentration of waves forms around the crack tip, as seen in Fig. D.24(g). These waves actively drive the crack bifurcation. Once bifurcation occurs (Fig. D.24(h)), the wave contributions originating from the crack tip become even more prominent, initiating complex internal wave patterns bounded by the bifurcated crack segments. With further crack development, P-waves emanate from both crack tips (Fig. D.24(i)). Here, a region with comparatively low wave intensity forms within the bifurcated zone, while the combined waves from the crack tips create a distinct new wavefront. Eventually, the specimen reaches full rupture, as illustrated in Fig. D.24(j).

Then, we focus on the dynamic SEN shear test, also analyzed using the 4th-order AT1 model and turn our attention to the propagation of S-waves due to the imposed shear loading history. Fig. D.25 shows the evolution of these waves. Upon application

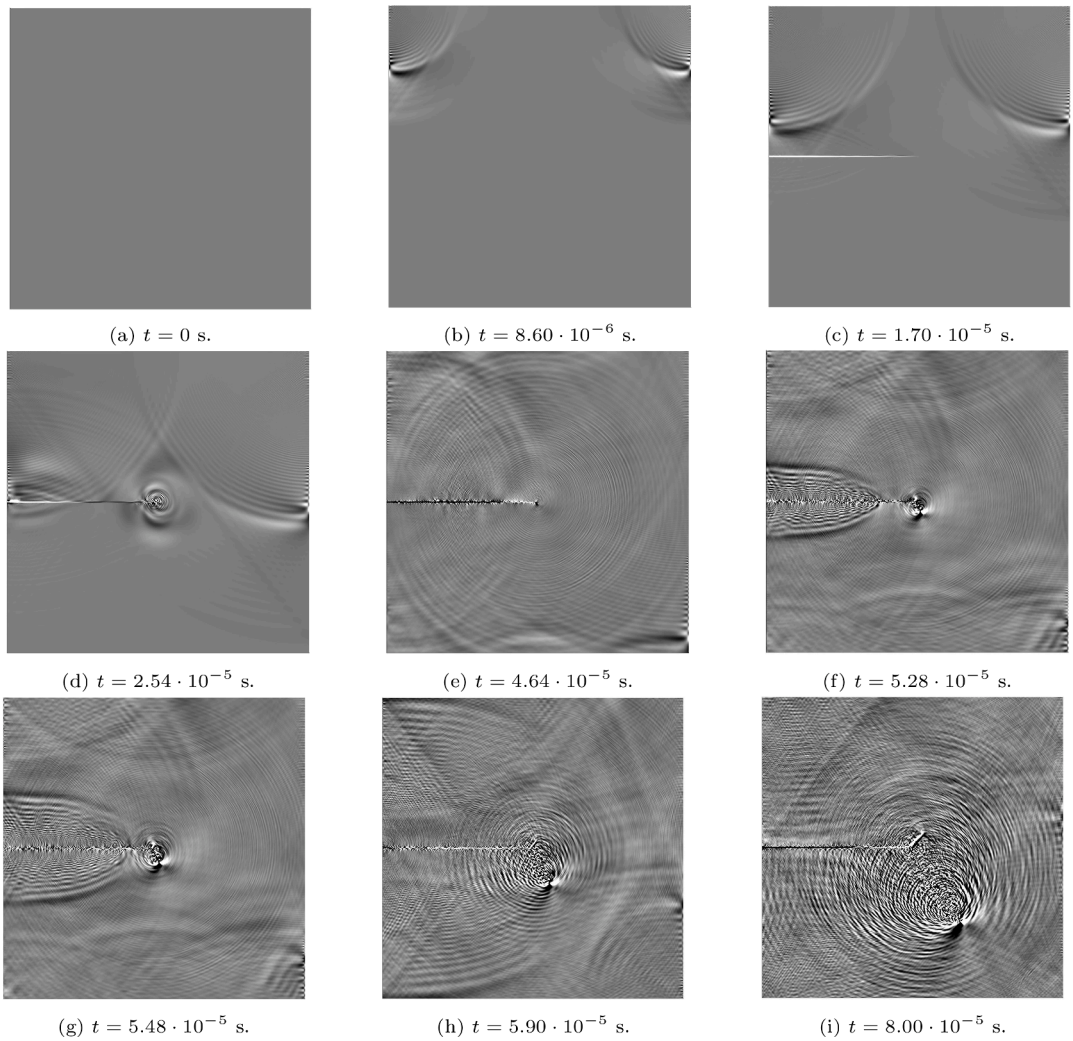

(a) $t = 0$ s. (b) $t = 8.60 \cdot 10^{-6}$ s. (c) $t = 1.70 \cdot 10^{-5}$ s.

(d) $t = 2.54 \cdot 10^{-5}$ s. (e) $t = 4.64 \cdot 10^{-5}$ s. (f) $t = 5.28 \cdot 10^{-5}$ s.

(g) $t = 5.48 \cdot 10^{-5}$ s. (h) $t = 5.90 \cdot 10^{-5}$ s. (i) $t = 8.00 \cdot 10^{-5}$ s.

Fig. D.25. Dynamic SEN shear test: relevant S-wave propagation instants in the fractured continuum for the 4th-order AT1 model.

of the shear load, S-waves start to propagate from the domain upper edges (Fig. D.25(b)) and travel towards the pre-existing crack (Fig. D.25(c)). Once the latters reach the crack tip (Fig. D.25(d)), new waves originate and expand upon interacting with the specimen boundaries, resulting in scattered waves that interfere with those already present in the domain (Fig. D.25(e)–(f)). As observed in Fig. D.25(g), the waves start traveling along the crack path, guiding the crack propagation diagonally in the direction of shear stresses. This leads to the formation of two crack branches (Fig. D.25(h)): a main downward branch and a shorter secondary upward branch, both generating additional waves from their respective crack tips.

References

[1] A.A. Griffith, G.I. Taylor, VI. The phenomena of rupture and flow in solids, Philos. Trans. Royal Soc. London. Ser. A, Containing Pap. Math. Phys. Charact. 221 (582–593) (1921) 163–198. https://doi.org/10.1098/rsta.1921.0006

[2] G.R. Irwin, Onset of fast crack propagation in high strength steel and aluminum alloys (1956).

[3] B. Bourdin, G.A. Francfort, J.-J. Marigo, Numerical experiments in revisited brittle fracture, J. Mech. Phys. Solids 48 (4) (2000) 797–826. https://doi.org/10.1016/S0022-5096(99)00028-9

[4] L. Ambrosio, V.M. Tortorelli, Approximation of functional depending on jumps by elliptic functional via t-convergence, Commun. Pure Appl. Math. 43 (8) (1990) 999–1036.

[5] M.J. Borden, T.J.R. Hughes, C.M. Landis, C.V. Verhoosel, A higher-order phase-field model for brittle fracture: formulation and analysis within the isogeometric analysis framework, Comput. Methods Appl. Mech. Eng. 273 (2014) 100–118. https://doi.org/10.1016/j.cma.2014.01.016

[6] T.J.R. Hughes, J.A. Cottrell, Y. Bazilevs, Isogeometric analysis: CAD, finite elements, NURBS, exact geometry and mesh refinement, Comput. Methods Appl. Mech. Eng. 194 (39) (2005) 4135–4195. https://doi.org/10.1016/j.cma.2004.10.008

[7] L. Greco, E. Maggiorelli, M. Negri, A. Patton, A. Reali, AT1 fourth-order isogeometric phase-field modeling of brittle fracture, Math. Models Meth. Appl. Sci. (2025). https://doi.org/10.1142/S0218202525500502

[8] M.J. Borden, C.V. Verhoosel, M.A. Scott, T.J.R. Hughes, C.M. Landis, A phase-field description of dynamic brittle fracture, Comput. Methods Appl. Mech. Eng. 217–220 (2012) 77–95. https://doi.org/10.1016/j.cma.2012.01.008

[9] S.F. Hosseini, M. Gorji, R. Sartorti, L. Radtke, A. DÃ¼ster, Simulating brittle fracture with a robust hybrid explicit–implicit solver for staggered phase-field problems, PAMM 25 (1) (2025) e202400042. https://doi.org/10.1002/pamm.202400042
[10] J. Chung, G. Hulbert, A time integration algorithm for structural dynamics with improved numerical dissipation: the generalized-α method J. of Appl. Mech. 60 (2) (1993) 371–375.
[11] G.M. Hulbert, J. Chung, Explicit time integration algorithms for structural dynamics with optimal numerical dissipation, Comput. Methods Appl. Mech. Eng. 137 (2) (1996) 175–188.
[12] H.L. Ren, X.Y. Zhuang, C. Anitescu, T. Rabczuk, An explicit phase field method for brittle dynamic fracture, Comput. Struct. 217 (2019) 45–56.
[13] A. Schlüter, A. Willenbücher, C. Kuhn, R. Müller, Phase field approximation of dynamic brittle fracture, Comput. Mech. 54 (2014) 1141–1161.
[14] T. Li, J.-J. Marigo, D. Guilbaud, S. Potapov, Gradient damage modeling of brittle fracture in an explicit dynamics context, Int. J. Numer. Methods Eng. 108 (11) (2016) 1381–1405.
[15] T. Li, J.-J. Marigo, D. Guilbaud, S. Potapov, Numerical investigation of dynamic brittle fracture via gradient damage models, Adv. Model. Simul. Eng. Sci. 3 (2016) 1–24.
[16] T.K. Mandal, V.P. Nguyen, J.-Y. Wu, Evaluation of variational phase-field models for dynamic brittle fracture, Eng. Fract. Mech. 235 (2020) 107169.
[17] A. Marengo, A. Patton, M. Negri, U. Perego, A. Reali, A rigorous and efficient explicit algorithm for irreversibility enforcement in phase-field finite element modeling of brittle crack propagation, Comput. Methods Appl. Mech. Eng. 387 (2021) 114137. https://doi.org/10.1016/j.cma.2021.114137
[18] L. Greco, A. Patton, M. Negri, A. Marengo, U. Perego, A. Reali, Higher order phase-field modeling of brittle fracture via isogeometric analysis, Eng. Comput. 40 (6) (2024) 3541–3560.
[19] H. Amor, J.-J. Marigo, C. Maurini, Regularized formulation of the variational brittle fracture with unilateral contact: numerical experiments, J. Mech. Phys. Solids 57 (8) (2009) 1209–1229. https://doi.org/10.1016/j.jmps.2009.04.011
[20] S. Goswami, C. Anitescu, T. Rabczuk, Adaptive fourth-order phase field analysis for brittle fracture, Comput. Methods Appl. Mech. Eng. 361 (2020) 112808. https://doi.org/10.1016/j.cma.2019.112808
[21] L. Piegl, W. Tiller, The NURBS Book, Springer Science and Business Media, (1996).
[22] J.A. Cottrell, T.J.R. Hughes, A. Reali, Studies of refinement and continuity in isogeometric structural analysis, Comput. Methods Appl. Mech. Eng. 196 (41) (2007) 4160–4183. https://doi.org/10.1016/j.cma.2007.04.007
[23] O.L. Mangasarian, Solution of symmetric linear complementarity problems by iterative methods, J. Optim. Theory Appl. 22 (4) (1977) 465–485.
[24] J.A. Cottrell, T.J.R. Hughes, Y. Bazilevs, Isogeometric Analysis: Toward Integration of CAD and FEA, John Wiley & Sons, (2009).
[25] T. Roubicek, C. Panagiotopoulos, C. Tsogka, Explicit time-discretisation of elastodynamics with some inelastic processes at small strains, (2019). arXiv preprint arXiv:1903.11654.
[26] E. Maggiorelli, M. Negri, Energy release and Griffith's criterion for phase-field fracture, EASIM Control Optim. Calc. Var. (2025). arXiv preprint arXiv:2502.10351.